UNIVERSIDAD NACIONAL AUTÓNOMA DE MÉXICO

POSGRADO EN CIENCIA E INGENIERÍA DE MATERIALES

SWIMMING OF MICROORGANISMS IN COMPLEX FLUIDS

T E S I S

QUE PARA OPTAR POR EL GRADO DE:
DOCTORA EN CIENCIA E INGENIERÍA EN MATERIALES

PRESENTA:

VERONICA ANGELES ESCUDERO

TUTOR:

Dr. José Roberto Zenit Camacho
Brown University

MIEMBROS DEL COMITÉ TUTOR:

Dr. Carlos Málaga Iguiñiz
Facultad de Ciencias

Dra. Catalina Elizabeth Stern Forgach
Facultad de Ciencias

Ciudad Universitaria, CD.MX, Octubre 2021

Acknowledgements

I am very happy to have spent five years in the Rheology department of Instituto de Materiales - UNAM. I would like to thank my advisor, Dr. Roberto Zenit, for his guidance, motivation, encouragement, patience, and support through my formation. Especially, to introduce me in the fantastic experimental world.

I also greatly appreciate the sustained and support from my committee and lab friends, Dr. Carlos Malaga, Dra. Catalina Stern, Dr. Carlos Palacios, Dr. Enrique Jeffroy, Dr. Marco Reyes, Dr. Federico Hernández, Dr. Francisco Godinez, Rogelio, Jorge, Bernardo, Elsa, Itzel, Erick, and recently Yunxing. I enjoyed our friendship and learned so much from them.

I am especially very grateful to Dr. Anton Maria Minzoni to introduce me in this adventure and cultivated my understanding in fundamental research about fluid dynamics. His particular sense of humor, encouragement, creativity, and wisdom I will never forget.

Finally, I would like to thank my parents, Olivar Angeles and Evelin Escudero, and my extended family, including my life partner Lauro, for their unconditional support and inspiration that pushed me in difficult moments.

I am thankful to CONACYT for give me a full grant during my studies.

Abstract

Fluids with complex rheological properties have an internal structure at molecular scale, however we experience them as homogeneous; which makes them a challenging subject of study. Most bacteria live in complex fluids and boundary conditions. Due to the environment in which they live, which make it a difficult problem to attack because there are many variables involved. Moreover, there are not general Navier-Stokes equations that describe complex fluids.

In this thesis, the behavior of artificial helical swimmers was investigated -conserving the Reynolds number- changing the fluid and the boundary conditions. Trying to simulate a common microorganism called *E. Coli* which is widely investigated for biomedical studies. I will focus mainly on three points: *(i)* the effect of fluid elasticity on swimming speed, *(ii)* effect of confinement (boundary conditions) on swimming speed for Newtonian and viscoelastic fluids, and *(iii)* the theoretical model of a helical swimmer in a granular medium. In this study a magnetically actuated helical swimmer was used. In essence, the swimmer's head has a magnet which is aligned with an external magnetic field. To generate a swimmer displacement, the external magnetic field has to rotate, so that the swimmer rotates around its axis.

In the study of the confined helical swimmer, we found that the swimming speed increases with a greater confinement. This behavior can be seen for both the Newtonian and the viscoelastic fluids. Furthermore, the swimmer's speed in the viscoelastic fluid is larger than for the Newtonian for all confinements. In addition, the swimming speed in viscoelastic fluids was studied. We found that depending of the geometry of the swimmer, the swimming speed may increase, decrease or remained unchanged. We proposed that such influence of viscoelasticity on the swimming speed may be explained by a "*snowman* " effect. Finally, the extension of the Theory of Resistive Forces for a granular medium considering a helical swimmer shows that it is a good approximation according to experimental comparison. The model captures the general behavior of the swimming speed. However, it does not predict the minimum conditions for the swimmer displacement and the angle at which the speed is maximum.

Resumen

Los fluidos con propiedades reológicas complejas poseen una estructura interna a escala molecular, sin embargo los percibimos como homogéneos, lo que los convierte en un tema de estudio desafiante. Debido a su entorno, la mayoría de las bacterias viven en fluidos y condiciones de frontera complejos, esto hace que entender su dinámica sea un tema difícil de atacar debido a las variables involucradas. Además, no hay ecuaciones generales de Navier-Stokes que describan a los fluidos con propiedades reologícas complejos.

En esta tesis se investigó el comportamiento de un nadador helicoidal artificial conservando el número de Reynolds constante, cambiando las pripiedades del fluido y las condiciones de frontera. Estos parámetros se ajustan tratando de simular un microorganismo común llamado *E. Coli*, ampliamente investigado en estudios biomédicos. Me enfocaré en tres puntos principales: *(i)* el efecto de la elasticidad del fluido en la velocidad de nado, *(ii)* el efecto del confinamiento (como condiciones de frontera) en la velocidad de nado para fluidos Newtonianos y viscoelásticos (Boger), y*(iii)* el modelo teórico de un nadador helicoidal en un medio granular. En este estudio se utilizo un nadador helicoidal accionado magnéticamente. En esencia la cabeza del nadador tiene un imán que se alinea con un campo magnético externo. Para generar el nado, el campo magnético externo rota de modo que el nadador gira alrededor de su eje.

En el estudio de nado confinado encontramos que la velocidad de nado se incrementa con el confinamiento. Este comportamiento se puede ver tanto para el fluido Newtoniano como para el viscoelástico. Además, para un mismo confinamiento la velocidad del nadador en el fluido viscoelástico es mayor que para el Newtoniano en todos los casos. También se observó que la velocidad de nado en fluidos viscoelásticos en algunos casos incrementa, en otros decrece o permanece sin cambio, dependiendo la geometría del nadador. Propusimos que esta influencia de la viscoelasticidad en la velocidad de nado puede estar controlada por un efecto de "*snowman*". Finalmente, la extensión de la teoría de fuerzas resistivas para medio granular considerando un nadador helicoidal, muestra que es una buena aproximación de acuerdo con los resultados de los experimentos. El modelo captura el comportamiento general de la velocidad de nado, sin embargo no predice las condiciones mínimas para que el nadador se desplace ni el ángulo en el cual la velocidad es máxima.

Contents

List of Figures

List of Symbols

Fluid Properties

μ	Viscosity for Newtonian fluids
η	Viscosity for Non-Newtonian fluids
ρ	Density

Fluid Dynamics

$\boldsymbol{u}$	Velocity vector
$\overline{D}$	Shear stress tensor ($\frac{\mu}{2}\dot{\gamma}$)
p	Pressure
$\boldsymbol{\sigma}$	Stress tensor
V	Swimmer velocity in x direction
τ	Relaxation time

Kinematic tensors

$\nabla \boldsymbol{u}$	Velocity gradient tensor ($\partial u_j / \partial x_i$)
$\dot{\boldsymbol{\gamma}}$	Rate-of-strain tensor $= (\nabla \boldsymbol{u} + (\nabla \boldsymbol{u})^T)$

Dimensionless Numbers

Re	Reynolds number
Wi	Weissenberg number
De	Deborah number

Geometrical parameters of the helical swimmer

λ	Helix wavelength
K	Wave number ($2\pi/\lambda$)
ω	Angular frequency
β	Helix angle
R	Helix radius
L_T	Tail length of the helical simmer
D_H	Head diameter
L_H	Head length

Publications

As part of the research work presented in this thesis the following publications were published:

1. Enhanced swimming speed of confined helical swimmers: unpublished
2. Front-back asymmetry controls the impact of viscoelasticity on helical swimming: published in Physical Review Fluids, 2020, vol. 6 , no 4. https://journals.aps.org/prfluids/abstract/10.1103/PhysRevFluids.6.043102
3. Self-propulsion of a helical swimmer in granular matter: published in Physical Review Fluids, 2019, vol. 4, no 8. https://link.aps.org/doi/10.1103/PhysRevFluids.4.084302

Part of this work was presented in

69th Annual Meeting of the APS Division of Fluid Dynamics, Session R21: Bio: Micro swimmers in November 22, 2016. **The swimming speed of a confined rotating helix in creeping flow.**

Chapter 1

Problem statement

Many types of motile cells adapt to their environment to survive. One type of locomotion is the flagella-based swimming of microorganisms such a *E. coli* whose tail adopts a helical shape. The understanding about how micro-swimmers move and stir the fluid that surrounds them is helpful for many applications. Micro-robots could be used to deliver drugs in a specific tissue or transporting and driving nano-machines through some media [1, 2, 3]. This understanding is also needed to better attack challenges including acute epidemics, persistent infection [4], and food spoilage and contamination [5].

Evidently, the comprehension of the microorganisms swimming in complex fluids is needed. In this work, we call complex fluids to those which are non-Newtonian. Fluids with complex rheological properties are usually homogeneous at the macroscopic scale and disordered at the microscopic scale, but possess structure at the intermediate scale. Examples include polymeric solutions, dense particle suspensions, and emulsions. These complex fluids often exhibit non-Newtonian properties under an applied deformation, such as viscoelasticity, yield-stress, and shear-thinning viscosity. Since this subject is quite extensive, we address only three aspects that affect the swimming speed of a helical swimmer: first, the effect of the viscoelastic fluid on the swimming speed. Second, the confinement on swimming speed in a Newtonian and complex fluid. Third, the effect of granular media on swimming speed.

1.0.1. Newtonian case

Our current understanding of locomotion at low Re number is derived mainly from investigations in Newtonian fluids. The Re number is the ratio between the inertial and viscous forces. The theoretical framework for micro-swimming mechanics in a Newtonian fluid was started with

investigations of idealized micro-swimmers like a sheet by Taylor [6] and flagellated cells by Hancock & Gray [7] integrating theoretical and experimental studies to explain the basic mechanism of sperm motility. Hancock developed a resistive-force theory (RFT) for slender-body theory in Stokes flow. The RFT captures the contribution of the fluid and the geometry's body. Both theories predict that the swimmer speed is proportional to the square of the wave amplitude.

Although the RFT approach is often satisfactory [8], it can be problematic for nontrivial flagellar interactions that occur in the presence of boundaries or even more in presence of boundaries in non-Newtonian fluid that is the closest case to the biological problem. There is a need of an investigation that address these interactions and explore how micro-swimmers respond through changes in their environment in a Newtonian and non-Newtonian fluid in order to know the effects of such as alterations in fluid rheology or the contributions of a boundary. All of these interactions are very important for applications such as fertilization [9] and biological problems.

1.0.2. Non-Newtonian case

In many cases, the micro-swimmer's locomotion occurs through environments that contain proteins and other polymers which display elastic, and non-Newtonian characteristics. Some examples include mucus transport by lung cilia [10] and spermatozoa swimming through the female reproductive tract. These complex fluids often have effects on the locomotion of microorganisms. A good example is the experiment carried out by Arratia *et al.* [11], they compared a human sperm in two complex fluids: cervical mucus with viscosity $\mu = 0.0007\,Pa.s$ and semen with viscosity $\mu = 0.14\,Pa.s$. They showed that the sperm swims at approximately the same velocity in both media despite the large variation of viscosities, see Figure 1.1. Also, they noted that human sperm flagellum beat with higher frequency but smaller amplitude and wavelength in cervical mucus compared to semen [11].

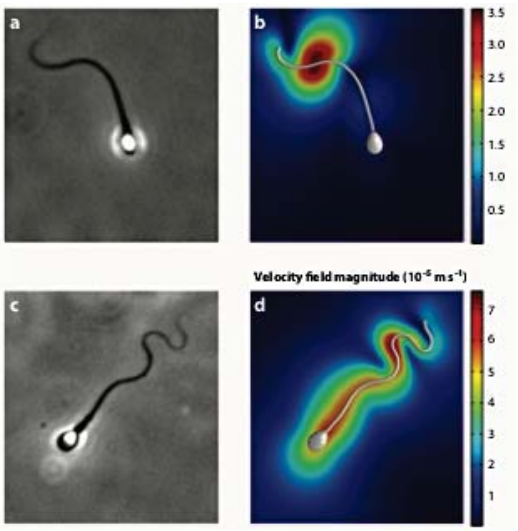

FIGURE 1.1: **(a,b)** Low-viscosity saline medium, with viscosity of 0.0007 Pa.s and **(c,d)** high viscosity saline-methilcellusose medium, with viscosity raised to 0.14 Pa.s. The sperm swims at approximately the same velocity in either medium, despite the large ratio of viscosities. Taken from Arratia (2014) [11].

The swimming theory in non-Newtonian fluids is much less developed than the Newtonian case. That is because for the non-Newtonian case the equations are highly non-linear, and hence classical Stokes flow methods involving superposition of fundamental solutions are invalid. Non-linearity appears due to a number of sources such as, the presence of time-dependent stresses, normal stress differences, and shear-dependent material functions in complex fluids. For example, viscoelastic fluids exhibit stress relaxation over time. The combined effect of both time scales the time required for relaxation and the periods of applied oscillatory stresses, as for a flagellum, introduce responses to the applied stresses that are out phase, as well as an in phase with them. Thus, the force distribution created by a motile flagellum will be affected by fluid viscoelasticity and the nature of the viscoelastic behavior will determine the swimming velocity [11].

For Newtonian fluids, only a single parameter is required to describe the rheological behavior: viscosity. And it only is used to correlate flow data one group of dimensionless variables, that number is the Reynolds number, Re. For viscoelastic fluids, the rheological behavior cannot be described by a single parameter, and two dimensionless groups are currently in use to correlate data for such materials. The Deborah number, De, governs the degree to which elasticity manifests itself in response to transient deformations. It is the ratio

of a characteristic time, τ, of the fluid to the duration of observation. Unless a deformation is very slow, the behavior of a viscoelastic fluid is strongly nonlinear, and the dimensionless group intended to describe the degree of nonlinearity is characterized by the Weissenberg number, *Wi*. It is the product of a characteristic time of the fluid and a characteristic rate of deformation [12].

There are some theoretical efforts to model a swimming speed in non-Newtonian fluids. Fulford *et al.* [13] extended the RFT theory for a viscoelastic fluid with a linear Maxwell model for viscoelasticity (as in Equation 2.45), and he did not find change in swimming speed compared with the Newtonian case. However, Lauga [14] showed that the swimming speed depends nonlinearly on wave amplitude and found that for a given wave pattern on a two-dimensional sheet, viscoelastic effects slow the swimmer relative to its velocity in a Newtonian liquid. In contrast, a two-dimensional numerical simulation for a finite undulating sheet using de Oldroyd-B model showed that fluid elasticity could in fact increase swimming speed when the beating frequency is equal to the inverse of the fluid relaxation time.

Additionally, the effects of fluid elasticity on microswimmers have been considered in computational studies on helical swimmers. Numerical simulations of swimmers with finite-length and large-amplitude showed that under some conditions, the swimming speed may be enhanced by elasticity [15]. Swimming speed has a maximum when the relaxation time of the fluid is similar to the period of the undulation. Other numerical simulations capture the effect of the walls in the swimming speed. Li and Spagnolie [16] investigated a helical swimmer inside a cylinder with different diameters. They found that the swimming speed can develop local maxima in the helical pitch, and the effects of confinement decrease exponentially fast with the tube diameter.

Despite of these recent efforts, there is still a lack of experimental investigations about swimming on viscoelastic fluids, the effects on fluid elasticity, and the effect of confinement on swimming is still not clear.

1.0.3. Granular case

Locomotion models have been developed for no-slip frictional materials like Newtonian fluids where it is possible to predict the propulsion speed because the swimmer interaction with the fluids is modeled by the Navier-Stokes equations with given boundary conditions. A new challenge is to understand the locomotion in other kinds of materials with a fluid-like behavior, for example: in sand, mud, etc. In these kinds of materials, there are not conservation equations to model the interaction between the boundary and the body at the level of Navier-Stokes equations [17, 18].

In particular, locomotion is less well understood in granular media due to its complex rheological features. The frictional nature of the particles results in yield stress, a threshold above which the grains flow in response to external forcing [17]. The resistance experienced by a moving intruder originates from the inhomogeneous and anisotropic response of the granular force chains, which are short areas affected grains surrounded [19]. At low locomotion speed and a granular media slightly polydisperse (to avoid segregation), where the granular matter is in a quasi-static regime, the effect of inertia is negligible compared to frictional and gravitational forces [20, 19], which is a regime similar to that of low Reynolds-number fluid.

Maladen *et al.* [21], inspired by RFT theory for locomotion in viscous fluids, developed an empirical RTF in locomotion of sandfish which moves in the subsurface undulating by a sinusoidal waveform. However, it is known that drag forces may differ depending on the physics which governs the body-medium interaction. For this reason, Maladen *et al.* [21] measured in granular substrates the forces perpendicular $F_{\perp}$ and parallel $F_{||}$ to the direction of movement for a slender cylinder and fitting some parameters. In this way, they obtained the analogous version of resistant coefficients for granular media. These functions were shown effective in modeling the undulatory subsurface locomotion of sandfish. Nevertheless, an interesting topic is missing to investigate: the influence of the geometry in the self-propulsion in granular media, in particular a helical swimmer. A recent study by Jung *et al.* [22] demonstrates that helical rotation is employed *Erodium* and *Pelargonium* seeds to penetrate cohesionless soils.

1.1. Objectives and structure of the thesis

After a review of the current literature, it is clear that many outstanding questions remain to be answered. The main aim of this thesis is to analyze experimentally and theoretically the behavior of a helical swimmer in complex media: granular media and Non-Newtonian fluids. Also, we analyze the differences in the velocity field when the swimmer is confined in Newtonian and non-Newtonian fluids.

1.1.1. Objectives for the confined case

1. Measure the speed for a helical swimmer in a Newtonian fluid and Non-Newtonian fluid in the confined case to compare the differences.

1.1.2. Objectives viscoelastic fluids

1. To mesure the speed for helical swimmers with different geometries and relative head sizes to quantify the influence of the swimmer geometry on the swimming speed.

2. Theoretically quantify the influence of the viscoelasticity and the tendency of the experimental swimmer speed.

1.1.3. Objectives for granular matter

1. Calculate theoretically the speed in granular media with and without head for a helical swimmer.

To serve these purposes, we investigate experimentally the effect on the swimming speed by the boundaries for Newtonian and Non-Newtonian fluids at low Re numbers with three different rotation frequencies in Chapter 3. This work is a complement of numerical simulations since no experiments have been conducted for this case. The experimental set-up is explained in Section 3.2. We found that the speed increases with the confinement for both fluids. Additionally, we found that the velocity is larger for the viscoelastic fluid (Boger) compared with the Newtonian one, see Section 3.3.2.

In Chapter 4, we explored the effects of the helical swimmer geometry on the swimming speed in a viscoelastic fluid. The experimental setup is explained in Section 4.2. It is found that the swimming speed is controlled

by the ratio of the head to helix size. This asymmetry of sizes induces a viscoelastic force that increases or decreases the locomotion, see Section 4.3.

Finally, in Chapter 5 we apply the analogy of RFT theory for a helix in a granular media in the free case and compare it with experimental results. This part exploits the application of RTF in granular media since there is a similar estimate for the speed but with a sinusoidal wave. We showed that RTF quantitatively describes well the movement of helical swimmers in granular media, see Section 5.3.

Chapter 2

General theory

In this chapter, we discuss relevant and general theories about swimming speed in Newtonian and Non-Newtonian fluids in the unconfined case. We start with a general theory about Newtonian fluids and the regime for microorganisms. Also, we develop the Resistive Force Theory applied for a helical swimmer. Then we discuss the general theory to model a viscoelastic fluid.

2.1. Locomotion at Low Reynolds number in Newtonian fluids

We will discuss the regime of Reynolds number that we consider for micro-swimmers. Then, we summarize the classical application of Newtonian fluid mechanics to flagellated cell swimming via slender-body theory and RFT.

The balance of momentum equations for an incompressible fluid describe the evolution of the velocity $\boldsymbol{u}(\boldsymbol{r}, t)$ of a fluid with density, ρ, dynamic viscosity, μ, a pressure gradient, ∇p, and a body force, $\mathbf{f}$ [23]:

$$\rho\left(\frac{\partial \boldsymbol{u}}{\partial t} + \boldsymbol{u}\cdot\nabla\boldsymbol{u}\right) = -\nabla p + \nabla\cdot\overline{D} + \boldsymbol{f} = 0. \tag{2.1}$$

For a Newtonian fluid the shear-stress $\overline{D}$ is linearly proportional to the fluid strain-rate $\dot{\boldsymbol{\gamma}}$. The constant of proportionality being the fluid shear viscosity μ such that $\overline{D} = \frac{\mu}{2}\dot{\gamma} = \frac{\mu}{2}[\nabla\boldsymbol{u} + (\nabla\boldsymbol{u})^T]$, where the superscript T represents the transpose tensor. The material derivate is defined as

$$\frac{D\boldsymbol{u}}{Dt} = \frac{\partial \boldsymbol{u}}{\partial t} + \boldsymbol{u}\cdot\nabla\boldsymbol{u}. \tag{2.2}$$

Dimensionless variables can be defined by choosing a characteristic length scale L and a characteristic velocity scale V,

$$\tilde{\boldsymbol{u}} = \frac{\boldsymbol{u}}{V}, \quad \tilde{\boldsymbol{x}} = \frac{\boldsymbol{x}}{L}, \quad \tilde{\nabla} = \nabla L, \quad \tilde{t} = \frac{V}{L}t, \quad \tilde{p} = \frac{p}{\mu V/L}.$$

In terms of the dimensionless variables, the balance of momentum equations become

$$\frac{\rho VL}{\mu}\left(\frac{\partial \tilde{\boldsymbol{u}}}{\partial \tilde{t}} + (\tilde{\boldsymbol{u}}\cdot\tilde{\nabla})\tilde{\boldsymbol{u}}\right) = \tilde{\nabla}\tilde{p} + \tilde{\nabla}^2\tilde{\boldsymbol{u}}. \tag{2.3}$$

Note that the body forces, were considered zero $\boldsymbol{f} = 0$. The terms on the left-hand side of this equation are the inertial effects. They describe the flow of momentum through the fluid. The second term on the right-hand side is the viscous term. This quantifies the dissipation on any velocity gradient. The balance of inertial and viscous contributions to a fluid's flow is described by the Reynolds number (Re), which follows from the coefficient of the viscous term in Equation 2.3

$$Re = \frac{\rho VL}{\mu} = \frac{\textit{inertial response}}{\textit{viscous response}} \tag{2.4}$$

where μ is the fluid viscosity. We can estimate the Re number for a micro-swimmers such as *E.coli* which swims in water. The viscosity of the water is $\mu = 1 \times 10^{-3}$ Pa·s and its density is $\rho = 1000$ kg/m^3, the characteristic length usually is $L \approx 2\times10^{-6}$ m and it is known the average velocity $V \approx 25\times10^{-6}$ m/s [24]. With this values and the Equation 2.4, the Reynolds number for this case is $Re \approx 5\times10^{-5}$. In general typical sizes from microorganisms are 10^{-5} m and velocities are 10^{-5} m/s giving $Re \approx 10^{-4}$ for swimming in water. Therefore, the Reynolds number is $Re \ll 1$, and thus we can assume the flow to be laminar. Additionally, we can consider the frequency-based Reynolds number, typically defined as

$$Re_{freq} = \frac{\rho L^2\omega}{\mu} \tag{2.5}$$

where $\omega \sim 100$ Hz is the frequency at which the bacterium flagella rotate, with this the $Re_{freq} << 0.1$ for *E. Coli*.
Then linear viscous forces rule the movement at small Reynolds number and the balance of momentum equations is reduced to the Stokes equations:

$$\tilde{\nabla}\tilde{p} = \tilde{\nabla}^2\tilde{\boldsymbol{u}}, \quad \tilde{\nabla}\cdot\tilde{\boldsymbol{u}} = 0, \quad \boldsymbol{x}\in\Omega, \tag{2.6}$$

where $\tilde{\boldsymbol{u}}$ is the velocity vector field in the domain Ω external to the swimmer.

The velocity is introduced in the model as a boundary condition $\tilde{\boldsymbol{u}} = \boldsymbol{V}$ for $\boldsymbol{x}$ on the swimmer boundary, where $\boldsymbol{V}$ denotes the speed of the boundary and thus represents no slip.
The Stokes equations are linear and therefore easier to solve than the Navier-Stokes equations. However, when the body boundary Ω is complex, like in the case of a helical swimmer, solving the Stokes equations analytically becomes a major challenge. One way to solve this problem analytically is with the Resistive-Force Theory (RTF) developed by Gray and Hancock [7].

2.2. Resistive-Force Theory (RFT)

At low Reynolds number, a rotating flagellum exerts an axial thrust F_{thrust} and a torque T related to the flagellum's axial velocity, V, and rotation rate, ω. The axial thrust is balanced by the drag forces of the helix, D_{helix}, and the head, D_{head}. If there are no external forces, it may be written as

$$F_{thrust} = D_{helix} + D_{head}. \tag{2.7}$$

However, until now we don't know any of these terms. To solve this problem, a theory called Resistive-Force theory was developed.

The essence of the propulsion mechanism for swimmers with flagellum was first described by Gray & Hancock [7]. The basis of the Resistive-Force Theory was stated by Hancock [25]. Their theory essentially requires that the drag coefficients associated with normal $K_\perp$ and tangential $K_\parallel$ motion satisfy $K_\perp / K_\parallel \approx 2$. Gray & Hancock fundamentally explained how a propagating flagellar wave produces a propulsive thrust that is balanced by the drag on the head. The Resistive-Force Theory can be interpreted as a logarithmically accurate local approximation that treats the ratio of the flagellum radius to its bending radius of curvature as a small parameter [26]. In other words, the RFT has better results for smaller helical angles.

Gray & Hancock assumed that the hydrodynamic forces experienced by the organism would be approximately proportional to the local body velocity. The force exerted by a body of flagellar segment, ds, with speed $V_\parallel$ in its tangential direction and speed $V_\perp$ in its normal direction experiences a local viscous drag approximately given by

$$\boldsymbol{F} = K_\perp V_\perp + K_\parallel V_\parallel, \tag{2.8}$$

where K corresponds to the local drag coefficient per unit length and it depends on swimmer geometry and fluid viscosity, $\perp$ and $\parallel$ are the normal and tangential components, respectively as shown in Figure 2.1.

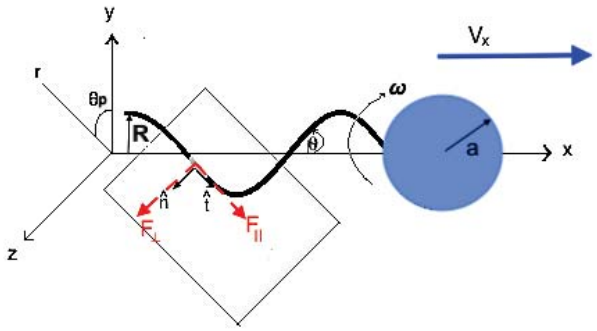

FIGURE 2.1: Normal and tangential vector on a differential element of the slender body. Helix with outer radius R and angle β with head radius a. Which moves with constant velocity in x axis V_x and rotation rate ω.

They developed this model for a microorganism that moves sinusoidally, such as *C. Elegans*. However, it can be implemented for the case of *E. Coli* which moves helically. Consider a swimmer in a Newtonian fluid that has a helical-slender flagellum with an outside radius R and a spherical head with radius a, see Figure 2.1. The swimmer has a constant velocity V along the x axis and an angular velocity ω. The parameterization of the helix is:

$$\boldsymbol{r}(x,t) = [x + Vt, R\cos(\theta), R\sin(\theta)]\,, \tag{2.9}$$

where $\theta = (kx - \omega t)$ and $k = 2\pi/\lambda$ is the wave number. Arranging this parameterization in cylindrical coordinates, we obtain

$$\boldsymbol{r}(x,t) = \left[(x + Vt)\widehat{\boldsymbol{e}_x} + R\widehat{\boldsymbol{e}_\rho}\right]. \tag{2.10}$$

We find the vector tangential to the helix

$$\widehat{\boldsymbol{t}} = \frac{1}{\sqrt{1 + R^2k^2}}[\widehat{\boldsymbol{e}_x} + Rk\widehat{\boldsymbol{e}_\theta}\big|_{\theta=kx}] = [\cos(\beta)\widehat{\boldsymbol{e}_x} + \sin(\beta)\widehat{\boldsymbol{e}_\theta}\big|_{\theta=kx}], \tag{2.11}$$

where β is the angle between the tangential vector and the x axis, it entails

$$\cos\beta = \widehat{\boldsymbol{t}}\cdot\widehat{\boldsymbol{e}_x} \;=\; \frac{1}{\sqrt{1 + R^2k^2}}, \quad \sin\beta = \frac{Rk}{\sqrt{1 + R^2k^2}} \Rightarrow \tan\beta = Rk. \tag{2.12}$$

Let $\boldsymbol{F}$ the Force vector acting on a differential arc length segment ds of the flagellum. This vector can be decomposed in the tangential direction plus a vector in a plane normal to the tangential vector as

$$\boldsymbol{F} = (\boldsymbol{F}\cdot\widehat{\boldsymbol{t}})\widehat{\boldsymbol{t}} + [\boldsymbol{F} - (\boldsymbol{F}\cdot\widehat{\boldsymbol{t}})\widehat{\boldsymbol{t}}]. \tag{2.13}$$

Then, we can define the unitary normal direction as

$$\widehat{\boldsymbol{n}} = \frac{\boldsymbol{F} - (\boldsymbol{F}\cdot\widehat{\boldsymbol{t}})\boldsymbol{t}}{\|\boldsymbol{F} - (\boldsymbol{F}\cdot\widehat{\boldsymbol{t}})\boldsymbol{t}\|}. \tag{2.14}$$

Therefore Equation 2.13 can be alternative written as

$$\boldsymbol{F} = (\boldsymbol{F}\cdot\widehat{\boldsymbol{t}})\widehat{\boldsymbol{t}} + \|\boldsymbol{F} - (\boldsymbol{F}\cdot\widehat{\boldsymbol{t}})\widehat{\boldsymbol{t}}\|\widehat{\boldsymbol{n}}, \qquad \widehat{\boldsymbol{t}} \perp \widehat{\boldsymbol{n}}. \tag{2.15}$$

Then, if we consider only the tangent and the normal components

$$F_{\parallel} = (\boldsymbol{F}\cdot\widehat{\boldsymbol{t}}) \qquad \text{and} \qquad F_{\perp} = \|\boldsymbol{F} - (\boldsymbol{F}\cdot\widehat{\boldsymbol{t}})\widehat{\boldsymbol{t}}\|, \tag{2.16}$$

we can rewrite any vector $\boldsymbol{F}$ as

$$\boldsymbol{F} = F_{\parallel}\boldsymbol{t} + F_{\perp}\boldsymbol{n}. \tag{2.17}$$

Combining Equation 2.11, Equation 2.17, and Equation 2.12 we obtain

$$F_{\parallel} = \cos\beta F_x + \sin\beta F_\theta, \quad F_{\perp} = \cos\beta F_\theta - \sin\beta F_x. \tag{2.18}$$

In matrix form any vector acting on one differential line segment ds can be written as

$$\begin{pmatrix} F_{\parallel} \\ F_{\perp} \end{pmatrix} = \begin{pmatrix} \cos\beta & \sin\beta \\ -\sin\beta & \cos\beta \end{pmatrix} \begin{pmatrix} F_x \\ F_\theta \end{pmatrix}, \tag{2.19}$$

Where F_x is the propulsion force and F_θ is associated with the torque force. The same decomposition can be applied for the velocity vector

$$\begin{pmatrix} V_{\parallel} \\ V_{\perp} \end{pmatrix} = \begin{pmatrix} \cos\beta & \sin\beta \\ -\sin\beta & \cos\beta \end{pmatrix} \begin{pmatrix} V_x \\ V_\theta \end{pmatrix}. \tag{2.20}$$

Using the linear relation between the Forces and Velocities given by Gray & Hancock in Equation 2.8 in matrix form, we find

$$\begin{pmatrix} dF_{\parallel} \\ dF_{\perp} \end{pmatrix} = \begin{pmatrix} K_{\parallel} & 0 \\ 0 & K_{\perp} \end{pmatrix} \begin{pmatrix} V_{\parallel} \\ V_{\perp} \end{pmatrix} \tag{2.21}$$

Combining Equation 2.21 and Equation 2.20, we obtain

$$\begin{pmatrix} dF_{\parallel} \\ dF_{\perp} \end{pmatrix} = \begin{pmatrix} K_{\parallel} & 0 \\ 0 & K_{\perp} \end{pmatrix} \begin{pmatrix} \cos\beta & \sin\beta \\ -\sin\beta & \cos\beta \end{pmatrix} \begin{pmatrix} V_x \\ V_\theta \end{pmatrix}. \tag{2.22}$$

We may substitute Equation 2.19 in Equation 2.22 to obtain an expression for the force in terms of the velocity (V_x, V_θ) and the resistant coefficients $(K_{\parallel}, K_{\perp})$ as

$$\begin{pmatrix} dF_x \\ dF_\theta \end{pmatrix} = \begin{pmatrix} K_{\parallel}\cos^2\beta + K_{\perp}\sin^2\beta & \sin\beta\cos\beta(K_{\parallel} - K_{\perp}) \\ \sin\beta\cos\beta(K_{\parallel} - K_{\perp}) & K_{\perp}\cos^2\beta + K_{\parallel}\sin^2\beta \end{pmatrix} \begin{pmatrix} V_x \\ V_\theta \end{pmatrix}. \tag{2.23}$$

Hence, the total propulsive force can be obtained by integrating the differential force dF_x over the entire flagellum length

$$F_x = \int_0^{s'} [\sin\beta\cos\beta(K_{\parallel} - K_{\perp})V_\theta + (K_{\parallel}\cos^2\beta + K_{\perp}\sin^2\beta)V_x]\, ds, \tag{2.24}$$

where ds is the arc length defined as $ds = \|r'(x)\|dx$. Combining Equation 2.9 and Equation 2.12 we obtain

$$ds = \|r'(x)\|dx \quad = \quad \sqrt{1 + R^2k^2}dx = \frac{dx}{\cos\beta}. \tag{2.25}$$

After applying this change of variable in Equation 2.24, we obtain

$$F_x = \int_0^{L_T} [\sin\beta(K_{\parallel} - K_{\perp})V_\theta + (K_{\parallel}\cos^2\beta + K_{\perp}\sin^2\beta)\frac{V_x}{\cos\beta}]\, dx, \tag{2.26}$$

where L_T is the helix length. Integrating with respect to x, the total propulsion force in the x direction due to the flagellum is given by

$$F_x = L_T\left[\sin\beta(K_{\parallel} - K_{\perp})V_\theta + \left(K_{\parallel}\cos\beta + K_{\perp}\frac{\sin^2\beta}{\cos\beta}\right)V_x\right] \tag{2.27}$$

Note that the anisotropy between the normal and tangential

drag coefficients, $K_\perp > K_\parallel$, is the origin of drag-based thrust [27]. In other words, supposse that $K_\perp = K_\parallel$ then balance force is $F_{xT} = K_\parallel(\cos\beta + \sin^2\beta/\cos\beta)V_x = 0$ which implies that $V_x = 0$ but it is not true because experimentally we see helix in movement. So, the anisotropy of resistant coefficients induces that force balance is not zero.Also, note that the only way in which a flapping velocity V_θ may lead to a net propulsion force is when $K_\perp > K_\parallel$. This is the condition for drag to induce propulsion.

Additionally, note that the RFT obtains the total force integrating the local forces on each small segment. The local forces are calculated using drag coefficients per unit length in the normal and tangential directions, so the RTF predicts the thrust and the drag on a flagellum. Then, the propulsion force in Equation 2.27 has two contributions: (1) the thrust and the (2) drag forces

$$F_{thrust} = L\sin\beta(K_\parallel - K_\perp)V_\theta, \quad D_{helix} = L\left(K_\parallel\cos\beta + K_\perp\frac{\sin^2\beta}{\cos\beta}\right)V_x \tag{2.28}$$

For an unconfined swimmer the resistance coefficients $K_\parallel$ and $K_\perp$ (per unit length) for a slender body with radius r_0 and length $2l$ are calculated analytically [28] as

$$K_\parallel = \frac{4\pi\mu}{2ln\left(\frac{2l}{r_0}\right) - 1} \quad \text{and} \quad K_\perp = \frac{8\pi\mu}{2ln\left(\frac{2l}{r_0}\right) + 1}. \tag{2.29}$$

If we consider the slender body hypothesis $l r_0$. The first coefficients of the Taylor series expansion are

$$K_\parallel \approx 4\pi\mu \quad \text{and} \quad K_\perp \approx 8\pi\mu. \tag{2.30}$$

Hence $K_\perp \approx 2K_\parallel$ in a first order. Now, we still approximation need to include the drag force contribution due to the head in the force balance, see Equation 2.7. It is known that for a spherical body with radius a, the drag force is $D_{head} = 6\pi\mu aV = DV$ [28]. With a balanced force between the thrust, F_{thrust}, and the drag, $D_{helix} + D_{head}$, forces is easy to find the velocity of the swimmer

$$V = \frac{L_T R^2 k\omega(K_\perp - K_\parallel)}{L_T R^2 k^2 K_\perp + L_T K_\parallel + D\sqrt{1 + R^2k^2)}}, \tag{2.31}$$

where the tangential velocity was taken as $V_\theta = R\omega$. Also we may rewrite the velocity in terms of the helix angle, β, according to Equation 2.12

$$V = R\omega \frac{(\varsigma - 1)\tan\beta}{1 + \varsigma\tan^2\beta + \dfrac{D}{K_\parallel}\dfrac{a}{L_T}\dfrac{1}{\cos\beta}}, \tag{2.32}$$

where $\varsigma = K_\perp / K_\parallel$.

2.3. Non-Newtonian fluids

A large number of liquid materials which behavior do not behave like Newtonian fluids, some examples include polymeric liquids, suspensions, surfactants, etc. These kinds of fluids have rather more complicated macroscopic properties and they are called non-Newtonian or even complex fluids. For example, a viscoelastic fluid exhibit the presence of memory, *i.e.* the stresses also depend on the flow history. Unfortunately, there is not a model analogous to the Navier-Stokes equations that describes momentum conservation of viscoelastic fluids. Usually, one may choose a model that is known to describe a particular type of fluid. In this section we describe two popular models used for diluted polymeric solutions that incorporate memory and stress anisotropy into constitutive equations. This section is based in these books: Leal [29], Macosko [30], Larson [31] and Spagnolie [27].

2.3.1. Maxwell's model

As mentioned the behavior of viscoelastic fluids is the result of two contributions: the elastic and the viscous response to forces. As a first approximation, we may think of a viscoelastic fluid as the linear combination of those responses. We can think in the simple shear deformation of a solid for the elastic response, and in the shear stress acting on a fluid for the viscous part.

The shear stress σ in an elastic solid produces deformations or changes in the strain γ. In the case of a small deformations this may be modeled using Hooke's law and can be written as

$$\sigma = G\gamma, \tag{2.33}$$

where G is the elastic constant of the material, also called shear modulus.
An analogous equation for the Newtonian viscous fluids is the linear

relationship between the stress σ and strain rate $\dot{\gamma}$:

$$\sigma = \eta\dot{\gamma}, \quad \dot{\gamma} = \frac{\partial\gamma}{\partial t}, \tag{2.34}$$

where η is the fluid viscosity for non-Newtonian fluids. It is important to note the distinción between the displacement gradient γ and the velocity gradient $\dot{\gamma}$. Due to similarities with Hook's law linear solids and liquids are often represented graphically by springs (elastic solid) and dashpots (viscous fluid), see Figure 2.2.

(a) (b)

FIGURE 2.2: Graphical depiction of elements in the two types of material response: a) a spring, elastic response b) a dashpot, viscous response.

The simplest model for a viscoelastic fluid with constant viscosity is the Maxwell model, where the configuration of the spring and the dashpot is one followed by the other as you can see in Figure 2.3. This model is the first approximation of the response of a viscoelastic fluid in one direction. However, to model the response of the material in all directions, a sum of springs and dampers is usually proposed to model a viscoelastic fluid.

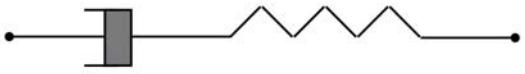

FIGURE 2.3: Ilustration of Maxwell linear viscoelastic model.

Imagine that this configuration is subjected to fixed displacements of their ends. The spring and the dashpot are stretched initially; however, the displacement of the spring can be redistributed to the dashpot, keeping the total displacement constant. To derivate the constitutive equations, we call the total deformation $\gamma = \gamma_s + \gamma_d$ and the total stress $\sigma = \sigma_s + \sigma_d$. Where the subscripts s and d correspond to deformation and stresses for the spring and dashpot respectively. The total deformation γ is the spring deformation (γ_s

elastic component) plus the dashpot deformation (γ_d viscous component)

$$\gamma = \gamma_s + \gamma_d. \tag{2.35}$$

So, the rate of deformation in time is

$$\dot{\gamma} = \dot{\gamma}_s + \dot{\gamma}_d \tag{2.36}$$

Considering the Equation 2.33, we have $\dot{\gamma}_s = \dot{\sigma}/G$. Additionally, the viscous contribution is given by $\dot{\gamma} = \sigma/\eta$, see Equation 2.34. So, it is easy to see that the constitutive equation for the Maxwell model are

$$\dot{\gamma} = \frac{1}{G}\dot{\sigma} + \frac{\sigma}{\eta}, \tag{2.37}$$

equivalently in terms of σ, we have

$$\eta\dot{\gamma} = \frac{\eta}{G}\dot{\sigma} + \sigma \tag{2.38}$$

Since the Maxwell model is linear, it is easy to analyze in terms of its response to a periodic deformation with frequency ω. Solving Equation 2.37 for a deformation $\gamma = \gamma_0 \sin \omega t$, we obtain

$$\begin{aligned} \sigma(t) &= \gamma_0 \eta \omega \left(\frac{\cos \omega t}{1 + (\tau\omega)^2} + \frac{\tau\omega_T \sin \omega t}{1 + (\tau\omega)^2} \right) \\ &= \frac{\eta}{1 + (\tau\omega)^2}\dot{\gamma}(t) + G\frac{(\tau\omega)^2}{1 + (\tau\omega)^2}\gamma(t) \end{aligned} \tag{2.39}$$

where $\tau = \eta/G$. So, the stress is decomposed into two waves of the same frequency: one in phase ($\sin \omega$) and other 90° out of phase ($\cos \omega$). Also, comparing the Equation 2.39 with equations Equation 2.33 and Equation 2.34 we can note that there are contributions due to a frequency dependent viscosity (proportional to $\dot{\gamma}$) and another due to shear modulus (proportional to γ).

Due to the elastic and viscous behavior, two functions are defined as the elastic (storage) modulus $G'(\omega)$ and the viscous (or loss) modulus $G''(\omega)$ given by

$$G'(\omega) = G\frac{(\tau\omega)^2}{1 + (\tau\omega)^2}, \quad G''(\omega) = G\frac{\tau\omega}{1 + (\tau\omega)^2} \tag{2.40}$$

In this sense, if a material satisfies $G' > G''$, we can say that is more elastic than viscous and viceversa. The crossover between the two regimes, $G' = G''$, occurs when the time scale of deformation is similar to the time scale of

relaxation, $\omega^{-1} \sim \tau$.

Equation 2.39 and Equation 2.40 are the basis of linear rheology. For small deformation amplitudes γ_0, we can measure the shear stress $\sigma(t)$, see Equation 2.39 and with it determines the viscosity, elastic modulus, and Maxwell relaxation time of the fluid. Linear rheological measurements are usually interpreted in terms of complex modulus, $G^*(\omega) = G'(\omega) + iG''(\omega)$, where i denotes the imaginary part of a complex number. Rheometers provide the storage and loss modulus as a function of ω and for Maxwell model the relaxation time can be determined as $\tau = \omega_0^{-1}$, with ω_0 as the frequency where $G'(\omega_0) = G''(\omega_0)$. However, the Maxwell model is often insufficient to describe even in linear rheology of polymeric solutions, and G' and G'' do not cross due to additional dissipation mechanisms. For example, if a viscoelastic material dissipates more energy than it stores implies that $G'' > G'$ and viceversa.

2.3.2. Oldroyd-B model

The Maxwell model has a physical problem: It is not frame-invariant. To show this, assume that we do the same experiment two times. The first time in a stationary lab frame, and in the second time with a constan velocity v_0 with respect to the lab frame. The stress components of the moving frame experiment should be written in terms of the lab frame coordinates as $\sigma_{ij}(\boldsymbol{x} + \boldsymbol{u_0}t, t)$. The time derivates become

$$\frac{\partial}{\partial t}\sigma_{ij}(\boldsymbol{x} + \boldsymbol{u_0}t, t) = \frac{\partial}{\partial t}\sigma_{ij} + \boldsymbol{u_0} \cdot \nabla\sigma_{ij} \tag{2.41}$$

We expected that both experiments should be described by the same equations since a there are not acceleration in the moving frame. Hence no additional stresses should be created in the fluid. However the time derivate in Maxwell model Equation 2.38 and Equation 2.41 differ by a term proportional to $\boldsymbol{v_0}$. So, this indicates that the Maxwell model is not frame-invariant [27].

To solve this complication, we need to define the upper convected derivates of a tensor as

$$\hat{\boldsymbol{A}} = \frac{D}{Dt}\boldsymbol{A} - (\nabla\boldsymbol{u})^T \cdot \boldsymbol{A} - \boldsymbol{A} \cdot (\nabla\boldsymbol{u}) \tag{2.42}$$

where $\hat{\boldsymbol{A}}$ is the upper-convected time derivative of a tensor $\boldsymbol{A}$, D/Dt is the material derivative, and $\nabla\boldsymbol{u}$ is the velocity gradient. In general, the

upper-convected time derivative is the change rate of some tensor property for a small element of the fluid that is written in the coordinate system rotating and stretching with the fluid. Then, the time derivatives in constitutive relations are generally written in this way to ensure that the parcels are frame-invariant. There are other frame-invariant choices, but the most popular, polymeric constitutive equations are formulated in terms of upper-convected time derivates.

The next simplest model of a polymeric fluid is the Oldroyd-B model. This constitutive equation is especially appropriate because it separates contributions of the solvent and the polymer. The Oldroyd-B equation is

$$\tau\hat{\boldsymbol{\sigma}} + \boldsymbol{\sigma} = \eta(\boldsymbol{\gamma} + \lambda_r\hat{\dot{\boldsymbol{\gamma}}}), \tag{2.43}$$

where $\boldsymbol{\sigma}$ is the stress tensor, $\boldsymbol{\gamma}$ is the deformation rate tensor, τ is the relaxation time, η is the viscosity, λ_r is the retardation time, and the $\hat{}$ denotes the upper convected time derivative, see Equation 2.42.

Equation 2.43 can also be considered as the combination of the constitutive equations for the solvent and the polymer. That is, the equation for the solvent stress $\boldsymbol{\sigma_s}$ is (see Equation 2.34)

$$\boldsymbol{\sigma}_s = \eta_s\dot{\boldsymbol{\gamma}}, \tag{2.44}$$

where η_s is the solvent viscosity. The equation for the polymer stress σ_p be given for the Maxwell model (see Equation 2.38)

$$\boldsymbol{\sigma}_p + \tau\hat{\dot{\boldsymbol{\sigma}}}_p = \eta_p\dot{\boldsymbol{\gamma}}, \tag{2.45}$$

where η_p is the viscosity due to the polymer. Adding the two stresses yields to the total stress $\boldsymbol{\sigma}$, the result is the Oldroyd-B model in Equation 2.43 with the retardation time estimated as $\lambda_r = \eta_s\tau/(\eta_s + \eta_p)$.
The Oldroyd-B model is one of the simplest models that provides a macroscopic hydrodynamic description of polymer solutions. The Oldroyd-B model qualitatively describes many features of the incompressible viscoelastic fluids (called Boger fluids, see Section 2.3.3). In a steady state simple shear flow, this constitutive equation predicts a constant viscosity, a first normal stress difference, and zero second normal stress difference [32].

2.3.3. Boger fluids

To simplify the problem theoretically, numerically, and experimentally for a complex fluid, we considered a particular fluid called Boger. A Boger fluid is a liquid that is elastic and has a constant viscosity which does not vary with shear rate. Nevertheless, most of the elastic liquids are polymer solutions; therefore, they are inherently shear thinning (*i.e.*, viscosity decreases with larger shear rates). However, Boger fluids are mixtures of very diluted polymer solutions such that viscosity variations with shear rate can be ignored [33].

Theoretically, numerically, and experimentally Boger fluids are important because we may separate elastic from viscous effects later on or afterwards. Such a separation is possible if the same experiment is conducted using two fluids: a Boger and a Newtonian fluid with the same viscosity. Therefore, differences measured at the same flow rate are the result from elastic effects alone. These kinds of fluids are modeled numerically and theoretically using the Oldroyd-B model, see Section 2.3.2.

A Boger fluid is usually modeled with the addition of many elastic modes associated with different relaxation times. Then, we may use the expression for the modulus in Equation 2.40, but with a series of relaxation times, τ_i. In other words, the elastic and the viscous modulus are estimated as the sum series

$$G'(\omega) = \sum_{i=1}^{N} G_i \frac{\tau_i^2 \omega^2}{1+\omega^2\tau_i^2}, \quad G''(\omega) = \omega\eta_s + \sum_{i=1}^{N} G_i \frac{\tau_i \omega}{1+\omega^2\tau_i^2}, \tag{2.46}$$

for low-amplitude oscillation at frequency ω. Where $G'(\omega)$ and $G''(\omega)$ are the new storage and loss modulus respectively; η_s is the Newtonian solvent viscosity, and G_i are the fitting parameters for each relaxation time τ_i. Using the method discovered by Baumgaertel and Winter [34] the coefficients G_i are determined as the minimum average square deviation (min, see Equation 2.47) between predicted G' and G'' values and measured data of $\bar{G}'$ and $\bar{G}''$.

$$\sum_{j=1}^{m} \left(\left[\frac{G'(\omega_j)}{\bar{G}'_j} - 1 \right]^2 + \left[\frac{G''(\omega_j)}{\bar{G}''_j} - 1 \right]^2 \right) = min, \tag{2.47}$$

where $\bar{G}'_j$ and $\bar{G}''_j$ are the measured data at m frequencies ω_j and G', G'' are calculated values from Equation 2.46.

To compute an average relaxation time $\langle\tau\rangle$, we need take in to account each mode $G_i\tau_i$ as in the next expression

$$\langle\tau\rangle = \frac{\sum_{i=1}^{N} G_i\tau_i^2}{\sum_{i=1}^{N} G_i\tau_i} \tag{2.48}$$

Chapter 3

Confined helix in viscoelastic fluids

3.1. Introduction

The flagellar actions that occur with confined boundaries in a non-Newtonian fluid are the closest to the biological problem. For example, micro-organisms swimming through permeable boundaries, cell walls, or micro-vasculature. Confinement is an environmental constraint that strongly influences the motion of micro-organisms.

The effect of solid boundaries on the swimming speed in viscoelastic and Newtonian fluids has been a topic of increasingly active research. We will mention some of them. For a Newtonian fluid, it has been calculated by Katz [35] and more recently pointed by others [36, 37, 38] that the swimmers can take advantage of walls to increase their motility. One the one hand, Felderhof [39] has shown that the speed for a Taylor sheet increases with confinement. On the other hand, Zhu [36] used a squirmer model to show that the velocity decreases with confinement the swimmer is pushed toward the wall. Liu *et al.* [38] analyzed a helical flagellum in a tube and found that the swimming speed increases monotonically as the confinement increases. However, Acemoglu *et al.* [40] adopted a similar model, They also accounted for the effects of the head and found a decrease in velocity with the confinement.

There have been some numerical efforts to model the effect of confinement. Through a numerical model for a helical ribbon, a filament, and a screw-in circular channels with radius R_{ch} under constant angular velocity Demir *et al.* [41] showed there is a positive influence of the confinement on the swimming velocity. Ledesma [37] reported on a dipolar swimmer in a rigid or elastic tube and found a speed enhancement due to the walls. Jana *et al.* [42] studied experimentally and numerically the swimming of *paramecium* inside a capillary tube. They showed that the microorganism executes helical

trajectories wich become in straight lines as the diameter of the capillary tube decreases. They found a stepped enhancement due to the confinement. This behavior has been reported for helical swimmers by other studies such as Liu *et al.* [38], Spagnolie [27], Bilbao, and Wu *et al.* [43].

Changes in fluid rheology or contributions due to the presence of boundaries are some of the effects that we need to address to be able to understand the dynamics of micro-swimmers. Understanding the behavior of confined micro-swimmers may also provide us a way to develop applications in micro-fluidic devices. It should be noted that an analytical expression for a confined swimmer in a viscoelastic fluid does not exists up to date.

In the following section we investigated the case closest to the biological problem. We experimentally address the effects on the swimming speed due to the presence of boundaries in Newtonian and non-Newtonian fluids.

3.2. Experimental set-up

A control experiment was carried out to verify analytic results for the free Newtonian case from Section 2.2. Also, we experimentally measured the swimming speed in a confined media for Newtonian and Non-Newtonian fluids. In this section, we describe how we measured swimming speed in a confined environment with rigid walls in Boger and Newtonian fluids.

3.2.1. Fluids

We considered two test fluids: the first was Newtonian with viscosity $\mu = 0.46\,Pa.s$ and density $\rho = 1384\,kg/m^3$. The second was a Boger fluid with density $\rho = 1340\,kg/m^3$, constant viscosity $\mu = 1.22\,Pa.s$, and average relaxation time $\tau = 0.47\,s$. This relaxation time was obtained fitting a Maxwell of four elements to the rheological test results (G' and G") following the method used by Baumgaertel [34], see Equation 2.47.

3.2.2. Helical swimmer

The swimmer was designed to fulfill the restrictions of the model described in the Section 2.2: its head is spherical and the wave-length of the helix is larger than its diameter. In other words, we make those assumptions to assure that

any element in the flagellum remains close to the center-line of the helix, and it allows a good approximation to the RFT theory.

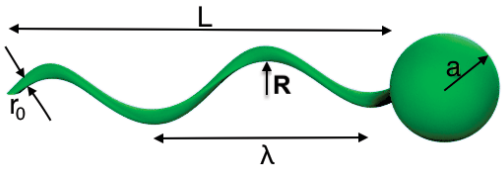

FIGURE 3.1: Geometric parameters of the helical swimmer with small curvature-arc. The helix has a radius R, wavelength λ, total length L_T, and the thickness of the helical filament is r_0. Additionally, the spherical head has a radius a.

The swimmer shown schematically in Figure 3.1 was 3D printed with ABS plastic (Young's modulus, $E = 2.6\,GPa$), and geometric parameters shown in Figure 3.1 and Table 3.1.

Geometrical characteristics of the swimmer		
		Units: [mm]
Tail	Wave length	$\lambda = 35.20 \pm 0.68$
	Total length	$L = 43.64 \pm 0.09$
	Exterior radius	$R = 3.15 \pm 0.68$
	Thickness	$r_0 = 0.79 \pm 0.07$
Head	radius	$a = 3.39 \pm 0.31$

TABLE 3.1: Geometrical parameters for the helical swimmer with spherical head.

A permanent cylindrical magnet and an air bubble were placed inside the head to have neutral buoyancy. The magnet is 3.18 mm both length and diameter and it has a remanent magnetic flux $B_m = 1.265 \pm 0.015$ T and density $\rho_m = 7450\ Kg/m^3$.

3.2.3. Magnetic device

We used the magnetically actuated helical swimmers designed by Godinez *et al.* [44]. In essence, a magnetized head driven by an external magnetic field experiences a torque aligns its magnetic field B_m with the external field B_e, see Figure 3.2(b). To generate an actuation, the magnetic field has to rotate, so the swimmer is rotated around its helical axis, see Figure 3.2(a). The external magnetic field, $B_e = 5.8\,mT$, was generated with a Helmholtz coil with radius

$R_{coil} = 140\,mm$, as described in detail previously [44]. Three rotation rates were considered: $1.46 \pm 0.5\ s^{-1}$, $1.96 \pm 0.6\ s^{-1}$, and $2.39 \pm 0.5\ s^{-1}$. A container (dimensions $15 \times 13 \times 14.5\,cm^3$) with test fluid was placed inside the coil as shown in Figure 3.2(a)

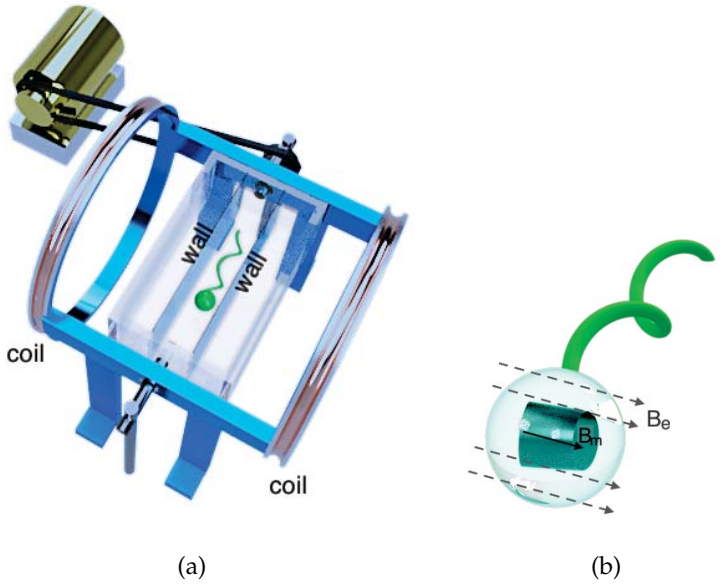

(a) (b)

FIGURE 3.2: Experimental setup used to propel a helical swimmer in a confined media. (a) Magnetic device: A pair of coils generate an external magnetic field B_e. The coils rotate with frequency ω and the confinement of the swimmer is by two parallel walls equally distant from the swimmer. (b) The external magnetic field B_e is aligned with the field B_m generated by a magnet inside the head of the swimmer to actuate the swimmer.

3.2.4. Confinement

The confinement was achieved by placing two thin parallel and equidistant layers, with distance h from the center-line, to the propeller axis as shown in Figure 3.3. A swimmer was placed in the container, and its motion was parallel to the walls, see Figure 3.2(a), until the swimmer had no propulsion due to the closeness of the walls. The swimming displacement was filmed with a digital camera at 30 fps. The images were digitally processed to obtain the swimmer's position and speed. Each experiment was repeated five times. A total of 16 confinement values were tested.

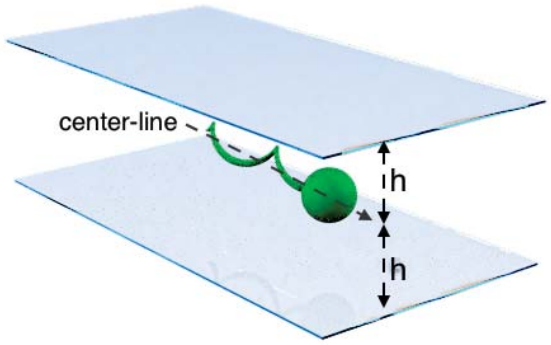

FIGURE 3.3: The confinement of the swimmer is given by two parallel walls with distance h from the center-line of the swimmer. The motion of the swimmer is longitudinally parallel to the walls.

3.3. Results and discussion

In this section, we considered the confinement effect in the swimming speed in both Newtonian and Boger fluids for three frequencies. As expected, the confinement and the fluid elasticity lead to changes in locomotion speed.

3.3.1. Newtonian fluid

We conducted measurements of the swimming speed in a Newtonian fluid without confinement, since we needed to corroborate the accuracy of the experimental technique and the agreement with the theoretical RTF prediction of Equation 2.31 [6, 7]. Consequently, the experiment was considered unconfined when $h/a = 4.81$, where a is the radius of the swimmer's head and h is the distance from the swimmer to the wall which in this case is the wall of the container, see Figure 3.2(a).

As shown in Figure 3.4 the swimmer speed increases with the rotating frequency ω, and the agreement with the theory is reasonable. Considering the geometry of the swimmer the solid line in pink color corresponds to the prediction of the resistive force theory in Equation 2.31.

Figure 3.5 shows the mean forward speed measured as a function of the confinement ratio, h/a, for the Newtonian fluid and with three different rotation speeds. At a given rotation rate, the swimmer speed progressively increases with confinements (as h/a decreases). The swimming speed in the most confined case, attained at $h/a \approx 3$, is approximately 25% faster than

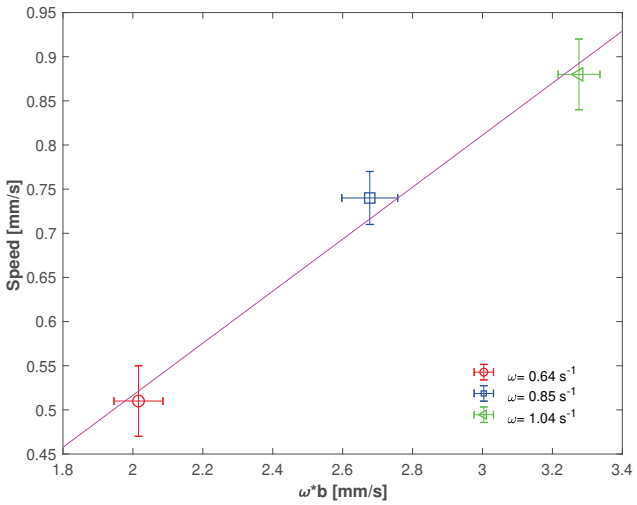

FIGURE 3.4: Swimming speed as a function of frequency: (○), $\omega = 0.64s^{-1}$; (□), $\omega = 0.85s^{-1}$; and (◁), $\omega = 1.04s^{-1}$. The line is obtained from Eqn (2.31).

the unconfined one, $h/a \approx 10$. The same behavior, was found with the three rotation speeds tested.

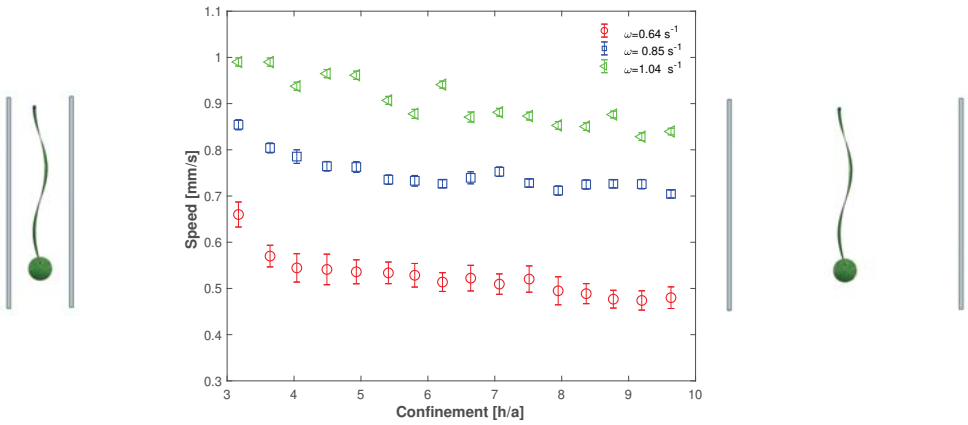

FIGURE 3.5: Swimming speed in Newtonian fluid as a function of confinement, h/a,for different rotational speeds: (○), $\omega = 0.64s^{-1}$; (□), $\omega = 0.85s^{-1}$; and (◁), $\omega = 1.04s^{-1}$. The sketches on the left and right correspond to the position of the walls with respect to the swimmer (confinement).

It is important to note that small values of h/a could not be tested because the swimmer rotation rate lagged behind the external rotation field. In other words, the magnetic torque was not sufficiently strong to maintain the swimmer "locked" with the external field. The confinement induces an increment in

the torque needed to rotate the swimmer at a given rate. Such cases were discarded.

3.3.2. Viscoelastic fluid

We show the results replacing the Newtonian fluid by a viscoelastic fluid (Boger) with nearly constant viscosity described in Section 3.2.1.

Figure 3.6 displays the measured mean speed V as a function of the confinement, h/a , for a Newtonian and a viscoelastic fluid (Boger). Filled symbols correspond to the Boger fluid while empty symbols are for the Newtonian one. The same swimmer was used under the same magnetic field and frequencies.

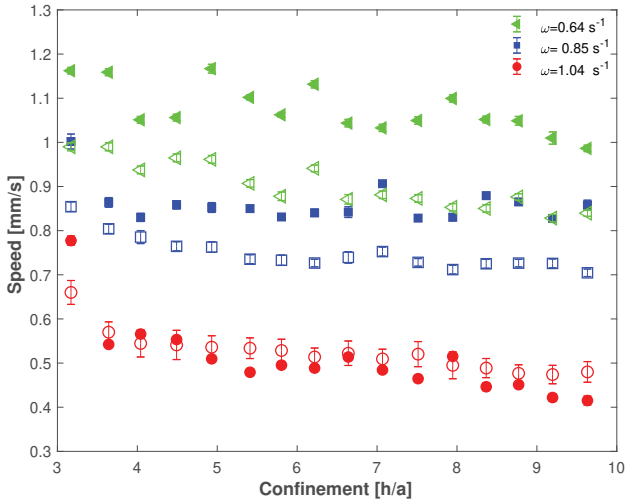

FIGURE 3.6: Swimming speed versus confinement in Newtonian (empty symbols) and non-Newtonian fluid (filled symbols) for three different frequencies: (○), $\omega = 0.64s^{-1}$; (□), $\omega = 0.85s^{-1}$; and (◁), $\omega = 1.04s^{-1}$.

First of all, for both fluids and all frequencies that we retested, the results are similar: the speed increases with confinement. However, the swimmer speed in the Boger fluid is above the speed in the Newtonian case for the two higher frequencies, while for the lowest frequency the speed is similar. The increment in speed with confinement is in agreement with the numerical results previously reported(E. Demir *et al.* [41], L. Li *et al.* [16], G. J. Li *et al.* [45], B. U. Felderhof *et al.* [39], and H. Wu *et al.* [43]).

Additionally, the effect of confinement on the speed for both fluids is small for $h/a > 6$. This threshold is important because we can get an estimated value of the distance between the swimmer and walls for which the walls do not affect too much the swimmer speed. As a consequence, in any other experimental set-up where the swimmer is considered free, the use of a container where the confinement is greater than 6 works as an unbounded domain. These results are also in good qualitative agreement with numerical results (L. Faucci *et al.* [46], R. Ledesma *et al.* [37], and B. Liu *et al.* [38]) and the theoretical prediction of D.F. Katz [35].

Figure 3.7 shows the speed in a Boger fluid as a function of Weissenberg number defined as $Wi = \tau \frac{V}{h}$ for each rotation frequency. Where τ is the relaxation time of the Boger fluid, V is the swimmer speed in the Boger fluid, and h is the distance from de swimmer to the walls, see Figure 3.3. The speed increases as the Wi increases for all the frequencies. It should be noted that in our case the Wi number increase because we changed the confinement, h, and with it the swimmer speed. However, the same result should be obtained if we change the fluid, *i.e* the relaxation time τ.

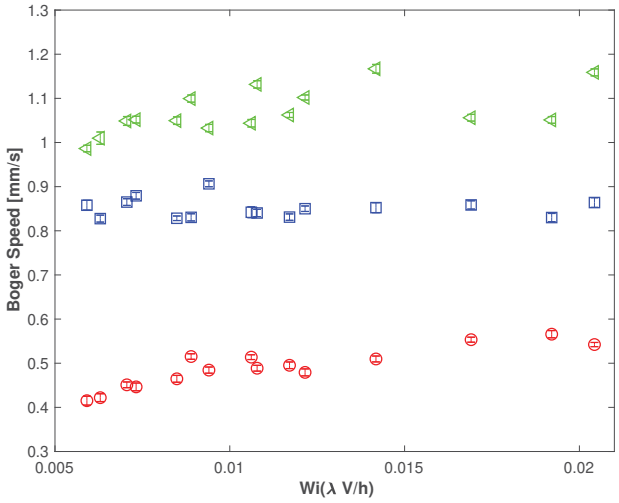

FIGURE 3.7: Swimming speed in a Boger fluid as a function of Weissenberg number for all the confinements. Each symbol corresponds to each rotation speed: (○), $\omega = 0.46s^{-1}$; (□), $\omega = 0.85s^{-1}$; and (◁), $\omega = 1.04s^{-1}$.

The Wi number is the ratio between elastic forces and viscous forces. So, for large Wi numbers the elastic energy stored in the fluid is greater than energy dissipated due to viscosity. In our case, the largest Wi number corresponds to

the most confined case, then we can say that the elastic energy increases in the fluid as the confinement does. In other words, the confinement induces larger shear rates (V/h) and thus produces a faster elastic response. Therefore, the fluid can store more elastic energy.

On the other hand, the Boger fluid experiences both viscous and elastic forces. The viscous force is the shear stress τ_{xy}. The dominant elastic force will be appear due to a new apparent force: the first normal-stress difference $N_1 = \tau_{xx} - \tau_{yy}$ that did not exist in Newtonian fluids. The Wi number is proportional to N_1, so when Wi increases the apparent force N_1 increases as well. It should be noted that N_1 has a component in the motion direction of the swimmer, *i.e.*, τ_{xx}. So, this may be why the speed is greater in the viscoelastic fluid compared with the Newtonian fluid.

The effect of viscoelasticity on the swimming dynamics is, in general, poorly understood. Contrasting results have been reported. For instance, F. A. Godinez *et al.* [47] found that swimmer speeds can be larger, smaller, or even equal than that in a Newtonian fluid, depending on the kinematics of swimming. On the other hand, S. E. Spagnolie *et al.* [48] reported that the swimming speed depended on the Deborah number and helix geometry.

In our case, it is clear that confinement below the threshold implies an increase in speed ratio. The confinement induces additional shear in the fluid which would produce a larger viscoelastic response of the fluid than an unconfined case, leading to a more pronounced effect on the swimming speed. This chapter shows that confinement could be an additional factor to be considered when analyzing the swimming speeds in non-Newtonian media. What we found in experiments is limited by confinement and the swimmer geometry. Future work should explore other confinement types, for example, an elastic or rigid cylindrical boundary as in [37]. Also, the effect of swimmer geometries in confined media could be analyzed.

3.4. Summary and Conclusions

In this chapter, we present an experimental investigation about the effect of the boundaries and elasticity on the swimming speed using a magnetically actuated swimmer.

Experimental results indicate that speed increases with confinement for all frequencies in both fluids: Newtonian and viscoelastic. Additionally, we find that fluid elasticity increases the propulsion of the helical swimmer. This trend is qualitatively similar to numerical and experimental results. Therefore, I expect an additional force when swimming in viscoelastic media to drive any speed increase.

Chapter 4

Helix in viscoelastic fluids

4.1. Introduction

Fluid embebed microorganisms exploit several methods to cope with the viscous effects or their surrounding environment dominated by viscous effects [49]. In particular, the majority of motile bacteria developed helical flagellar filaments to achieve locomotion [50]. These semi-rigid filaments can be used either in isolation (monotrichous bacteria) or for cells with several helical filaments (peritrichous bacteria); they may bundle together to form a single helical structure. In all cases, propulsion of the cell is enabled by the rotation of a helix in the viscous fluid: since a helix is chiral, a rotation around the helical axis bypasses the constraints of the scallop theorem [51] leading to a viscous thrust along its axis.

The mechanics of helical swimming is well understood in the case of Newtonian flows [52]. However, many of the fluids in which microorganisms move are not Newtonian, ranging from mucus and complex suspensions to biological tissues. When such a complex fluids are involved, the dynamics of swimming microorganisms is significantly affected by viscoelasticity, the presence of shear-dependent stresses, or both. Numerous studies have been devoted to the subject [14, 53, 54, 55, 56, 57, 48, 47]. Some results appear to be in contradiction with each other, and thus a number of fundamental issues remain unsolved.

There are some theoretical efforts that consider the elastic contributions of the fluid. Chaudhury [58] attempted to incorporate the effects of fluid elasticity on locomotion using a series of expansions. He predicted that fluid elasticity could either increase or decrease the propulsion speed of the waving sheet depending on the value of Re. Later, the effects of elasticity on beating flagellar structures were considered in the Stokes flow regime using the Maxwell model

with Equation 2.45 [13]. It was shown that self-propulsion was not affected by viscoelasticity even at large Deborah numbers ($De = \lambda\omega$), where λ is the fluid relaxation time and ω is the beating frequency. However, the total work decreased with increasing De. Then, it was suggested that a microorganism could swim faster in a viscoelastic fluid with the same expenditure of energy compared with a Newtonian fluid.

More recently, Riley & Lauga [59] showed that for a waving sheet like-Taylor sheet inside a viscoelastic fluid, elastic stresses could alter the speed U according to the equation

$$\frac{U}{U_N} = \frac{1 + De^2\,(\eta_s/\eta)}{1 + De^2}, \tag{4.1}$$

for small amplitude swimming and using the Oldroyd-B model in equations Equation 2.43, where U_N is the Newtonian speed and η_s is the solvent viscosity. While $\eta = \eta_s + \eta_p$ where η_p is the polymer viscosity. If we consider diluted solutions (such a Boger fluid) *i.e.*, $\eta_s/\eta < 1$, then $U \leq U_N$ for $De \ll 1$. In other words, the velocity in the viscoelastic fluid is lower than in the Newtonian fluid.

The effects of fluid elasticity on the swimming behavior were experimentally investigated by X. Shen *et al.* [54], they found that fluid elasticity hinders self-propulsion. Compared to Newtonian solutions, fluid elasticity leads to up to 35% slower propulsion as shown in Figure 4.1. Figure 4.1 shows the swimming speed, U, normalized by Newtonian speed, U_N, as a function of Deborah number. Experimental data, squares, show that speed decreases as elasticity in the fluid increases. The dotted line corresponds to numerical simulations of Teran *et al.* [15] that is discussed below. The solid line shows the general trend from the model of Riley & Lauga [59] using Equation 4.1, and the dashed line corresponds to predictions of Riley & Lauga [59] using the experimental data by X. Shen.

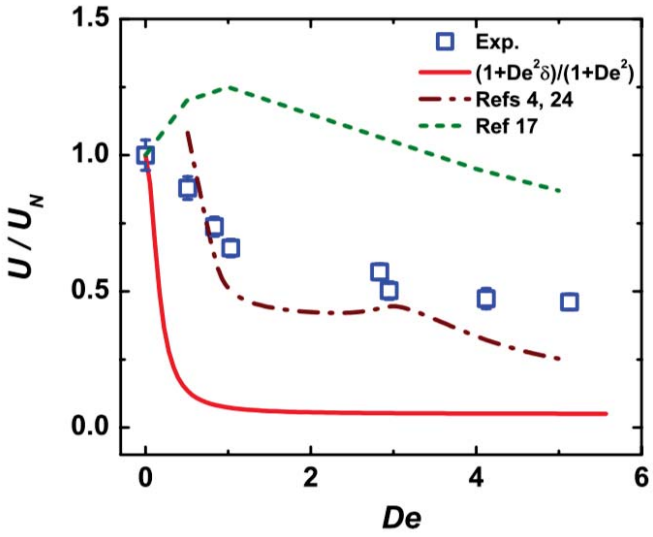

FIGURE 4.1: Swimming speed normalized by Newtonian Speed U_N for a *C.Elegans* as a function of Deborah number. The experimental data, squares, show that propulsion speed decreases as Deborah number. The solid line shows the general trend using a model of Equation 4.1. The dashed line corresponds to prediction of Equation 4.1 with experimental data. Taken form X. Shen (2010).

Also, they show that the self-propulsion decreases as elastic stresses grow in magnitude in the fluid, and they related that decrease with the stretching of flexible molecules near hyperbolic points in the flow.

Numerical simulations have also been used to address the effect of elasticity on swimming behavior. Teran *et al.* [15] considered a free sheet swimming in a viscoelastic fluid (Oldroyd-B fluid, Equation 2.43), along which moves a wave with small and large amplitudes. The simulation shows that the sheet increases its velocity as the Deborah number, De, increase and has a maximum in $De \approx 1$ for large amplitudes. For $De > 1$ the swimming speed decreases as De increases, see Figure 4.2 where the De vs the ratio of average swimmer speed to Newtonian speed, R, is shown. For small-amplitudes results for infinite sheets suggest that viscoelasticity impedes locomotion as Riley & Lauga showed.

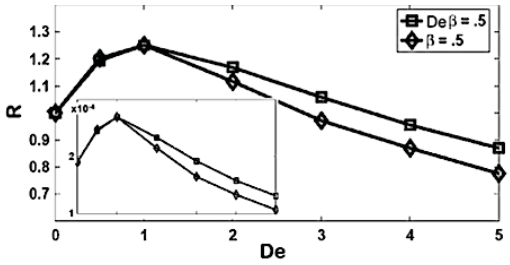

FIGURE 4.2: The ratio of average swimmer speed to Newtonian speed (R) as a function on *De*. βDe is the ratio of polymer to solvent viscosity, the limit $De \to 0$ yields a Newtonian fluid. Taken form Teran (2010).

An important experimental result measured on artificial swimmers is the dependence of propulsion speed on the geometry of the waveform and the fluid elasticity or Deborah number. Liu *et. al.* [53] measured the speed of two rotating rigid helixes in two viscoelastic fluid (Boger fluid). They found that the swimming speed increases relative to the viscous speed reaching a peak when the relaxation time is comparable to the rotation period as shown in Figure 4.3.

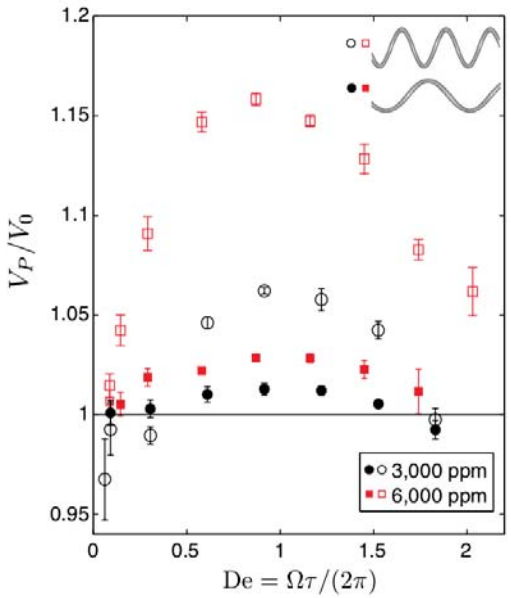

FIGURE 4.3: Ratio of free-swimming speed in viscoelastic fluid V_p to that in the Newtonian fluid V_0, as a function of the Deborah number De, for two different polymer solutions and two different helices.

Other geometries are explored to design a propeller able to move in only complex fluids. For example, two linked spheres rotating at the same angular

speed as a rigid body, as shown in Figure 4.4. This setup is called "snowman" which propels under an external torque.

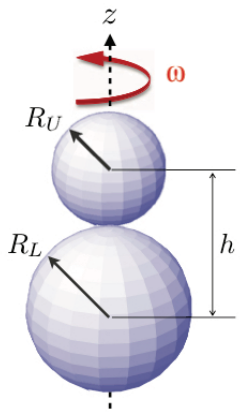

FIGURE 4.4: Geometrical setup of "snowman": two spheres rotating with angular velocity ω along their axis. The radii of the upper and lower spheres are denoted by R_U and R_L respectively. Taken from Pak *et. al.* (2012) [60].

The snowman was model by Pak *et al.* [60] for two aligned rotating spheres at the same speed as a rigid body, see Figure 4.4. Pak [60] shows that the velocity in a viscoelastic fluid is:

$$\frac{U_{elastic}}{\omega R_L} = De(1-\xi)\frac{2r^{*3}(1-r^*)}{(1+r^*)^6} \tag{4.2}$$

where r^* is the ratio of the radius of the upper sphere to the radius of the lower spheres $r^* = R_U/R_L$, ω is the rotation frequency, De is the Deborah number and ξ is the relative viscosity $\xi = \eta_s/\eta$ where $\eta = \eta_s + \eta_p$. This equation is a second-order expansion of an Oldroyd-B fluid for small Deborah numbers. In Figure 4.5 shows the propulsion speed as a function of r^*. The dotted line represents Equation 4.2, the red points are the numerical results in an Oldroyd-B fluid. Note that the optimal sphere size occurs at $r^*_{opt} \sim 0.58$.

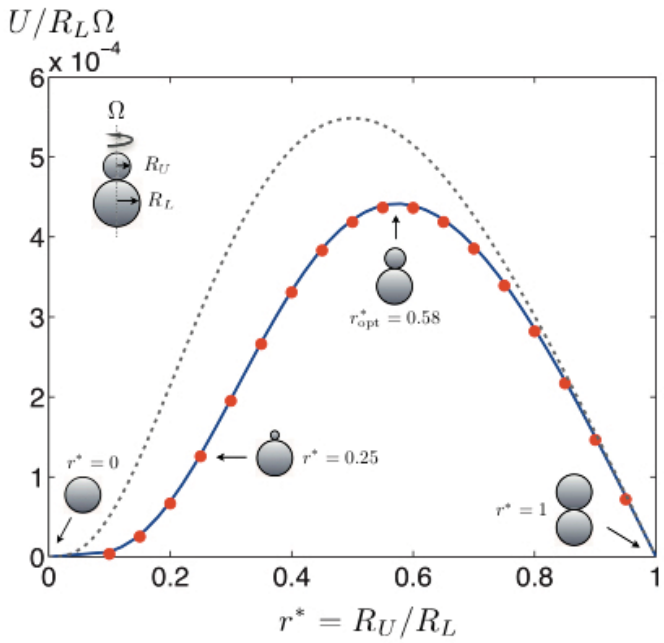

FIGURE 4.5: Propulsion speed of snowman as a function of the ratio $r^* = R_U/R_L$ at De=0.1 and $\xi = 0.5$. Red dots: numerical results. Dotted line: analytic model of Equation 4.2. Taken from Pak *et al.* (2012) [60].

It should be noted that the velocity goes to zero when $r^* = 1$, the two spheres have the same radius, and $r^* = 0$, there is only one sphere, as shown in Figure 4.5. Also, elastic effects tend to produce a secondary flow in opposite directions. We can see this effect, see Figure 4.5, where the snowman should swim faster or slower depending on the position of the small sphere.

Therefore, in addition to the expected dependence on the value of the Deborah number, the geometrical properties of the swimmer have a significant impact on the free-swimming speed in a non-Newtonian fluid. The biological example where the shape is known to be essentially rigid and unchanged by the fluids is the rotating helical filaments of swimming bacteria. In the Newtonian limit, the dynamics of a swimming rotating helix is well understood and characterized [28, 25, 51].

In this section, we conduct experiments to measure the swimming speeds for helices with many different geometries and relative head sizes.

4.2. Experimental set-up

The experimental design is similar to that previously used in Section 3.2.3. A force-free magnetically swimmers are used, so the swimmers can be rotated under the action of an external rotating magnetic field.

4.2.1. Helical swimmers

Ten swimmers were used with different head and helices sizes. Its head is cylindrical with length L_H and diameter D_H. The helical tail has a wavelength λ, radius R, the thickness of the helical filament r_0, and total length L_T as shown in Figure 4.6.

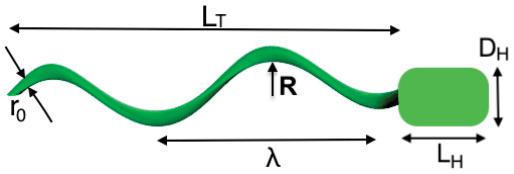

FIGURE 4.6: Geometric parameter of the magnetically-driven helical swimmer. The helix has a radius R, wavelength λ, total length L_T, and the thickness of the helical filament is r_0. Additionally, the head has a length L_H, and diameter D_H.

Table 4.1 shows the geometrical parameters of the 10 swimmers. The empty and full symbols correspond to experimental points for Newtonian and Boger fluids in the following figures. It is important to note that the head size, D_H, remains relatively constant for all swimmers. However, to achieve different pitch angles, the helix size, $2R$, varies significantly. Therefore, the ratio $D^* = 2R/DH$ varies from 0.6 to 3.93. In other words, the helix diameter may be smaller, $D^* < 1$, or larger, $D^* > 1$, than the head diameter as shown in Figure 4.7.

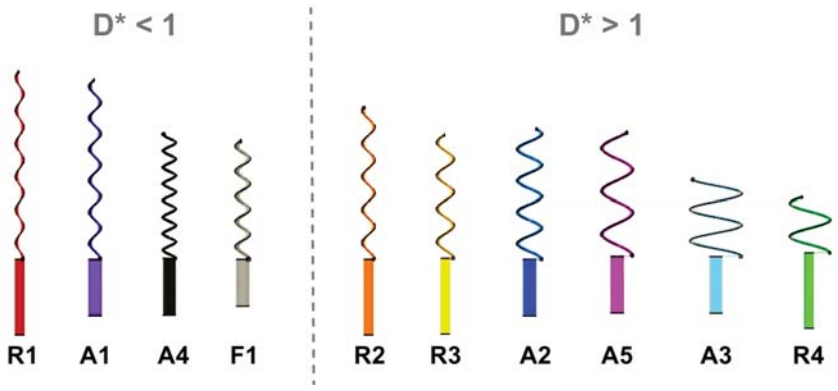

FIGURE 4.7: Sketch of the ten swimmers. The helix diameter may be smaller, $D^* < 1$, or larger, $D^* > 1$, than the head diameter.

Geometrical parameters of the swimmers							
Swimmer Units	L_H [mm]	D_H [mm]	r_0 [mm]	λ [mm]	2R [mm]	L_T [mm]	$D^* = \frac{2R}{D_H}$
R1 (○, ●)	23	3.0	0.9	10	1.8	56.8	0.6
A1 (◁, ◀)	17.3	4.1	1.0	9.5	3.0	54.3	0.73
A4 (○, ●)	17.3	4.1	1.0	5.0	3.5	37.6	0.85
F1 (△, ▲)	14.3	4.0	0.3	7.6	3.5	35.7	0.88
R2 (□, ■)	23	3.0	0.9	10	3.2	45.9	1.07
R3 (▽, ▼)	23	3.0	0.9	10	4.6	37.3	1.53
A2 (▷, ▶)	17.3	4.1	1.0	9.5	7.0	39.36	1.71
A5 (□, ■)	17.3	4.1	1.0	13.0	9.0	37.2	2.20
A3 (△, ▲)	17.3	4.1	1.0	9.5	15.0	23.2	3.66
R4 (◊, ♦)	23	3.0	0.9	10	11.8	16.8	3.93

TABLE 4.1: Geometrical parameters for ten helical swimmers. The empty and full symbols represent experiments in Newtonian and Boger fluids respectively in following figures.

Also, a permanent magnet and air bubble were placed inside the head to have neutral buoyancy. The magnet is 3.18 mm in length and diameter and it has a remanent magnetic flux $B_m = 1.2650.015$ T.

4.2.2. Fluids

Two types of fluids were used, a Newtonian and a viscoelastic Boger fluid, and we used two test fluids with different properties in each case. The rheological properties of the fluids were determined using a rheometer with parallel plates with 40 mm diameter and 1 mm gap (TA Instruments, ARES-G2). Both steady and oscillatory tests were conducted to measure the dynamic viscosity, μ, the storage and loss moduli, G′ and G″, respectively. The mean relaxation time, λ, is calculated by fitting G′ and G″ to a generalized Maxwell model [34]. The density ρ of the fluids was obtained using a 25 ml pycnometer. Table 4.1 shown the fluid rheological properties.

Rheological properties of the fluids				
Fluid Units	ρ $[kg/m^3]$	μ $[Pa \cdot s]$	n	τ $[s]$
N1	1390	3.5	1	0
N2	1385	1.64	1	0
B1	1340	3.8	0.98	1.23
B2	1366	1.64	0.98	1.63

TABLE 4.2: Rheological properties of the four fluids: two Newtonian (N1, N2) and two Boger (B1, B2) fluids. Where ρ is the density, μ dynamic viscosity, n power index, and τ fluid relaxation time.

4.3. Results and Discussion

In Figure 4.8, we show three typical experimental results chosen to illustrate the three possible qualitative results. The swimming speed is plotted as a function of the rotational frequency ω for swimmers F1, R1, and R4 from Table 4.1 for the first fluid pair N1 and B1, see Table 4.2. Empty and full symbols correspond to Newtonian fluid and Boger fluid respectively.

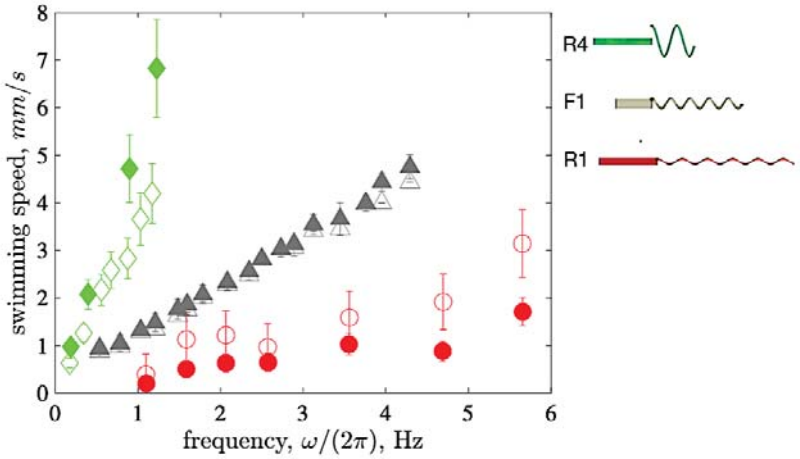

FIGURE 4.8: (Left) Swimming speed as a function of rotational frequency ω, for three representative swimmers (F1, R1 and R4 see Table 4.1). Empty and filled symbols represent the results for Newtonian, $N1$, and viscoelastic ,$B1$, fluids respectively (see Table 4.2). (Right) Sketch of the three swimmers: F1, R1, and R4 which shows that the helix diameter can be smaller or larger than the head diameter.

Clearly, for a helical swimmer three different behaviors are possible. The swimmer can swim faster (green rhombus), slower (red circles), or approximately with the same speed (grey square) in a viscoelastic fluid compare to the Newtonian case. The three swimmers, despite the changes in their geometrical parameters, are propelled by the same helical action, and the most notable difference between them is the value of the ratio between the sizes of the head and helical radius, $D^* = 2R/D_H$, which ranges from 0.63 -slower swimming to 3.93 degrees -faster swimming-.

To quantify the influence of viscoelasticity on the locomotion, we next calculate the ratio of the swimming speeds, U_{NN}/U_N, where U_{NN} and U_N are the measured mean speeds in the viscoelastic and Newtonian fluids, respectively. To assess the relative importance of viscoelastic effects, we calculate the Deborah number as $De = \omega\tau$, where τ is the fluid relaxation time (from Table 4.2). The ratio U_{NN}/U_N is plotted in Figure 4.9 as a function of Deborah number for all the swimmers studied here (from Table 4.1). Despite the large range of Deborah numbers in our experiments (from below 1 to above 20), a clear trend is not apparent in the data.

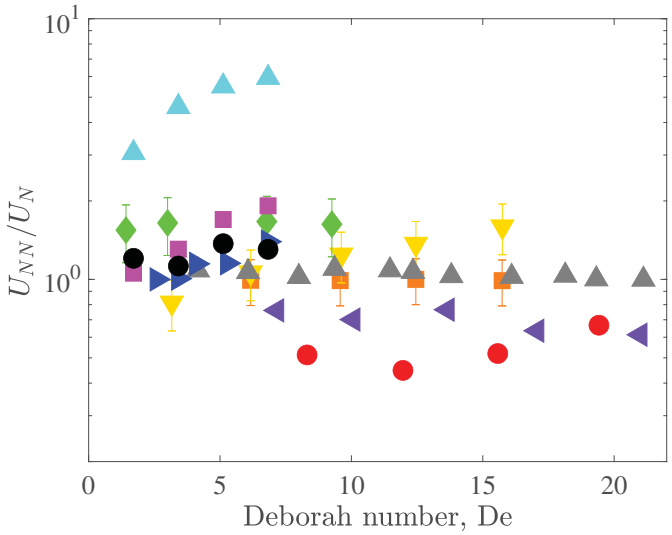

FIGURE 4.9: Ratio of viscoelastic swimming speed between viscoelastic and Newtonian fluids, U_{NN}/U_N, as a function of Deborah number, $De = \omega\tau$.

Instead of the Deborah number, one could argue that the relevant parameter to interpret the data is the Weissenberg number, Wi, which, instead of comparing the relaxation time of the fluid with the rotation rate of the swimmer, compares it to the relative rate of deformation in the flow. Hence, we can

define Wi as $Wi = \dot{\gamma}\tau$, where $\dot{\gamma}$ is the characteristic shear rate. For a rotating helix, the shear rate scales as $R\omega/\lambda$. Therefore, we have $Wi \sim (R/\lambda)De$. We plot in Figure 4.10 the normalized mean speed, U_{NN}/U_N as a function of the Weissenberg number for all experiments. These dimensionless numbers can therefore not be used alone to characterize the cadges in swimming speed when viscoelastic effects are present.

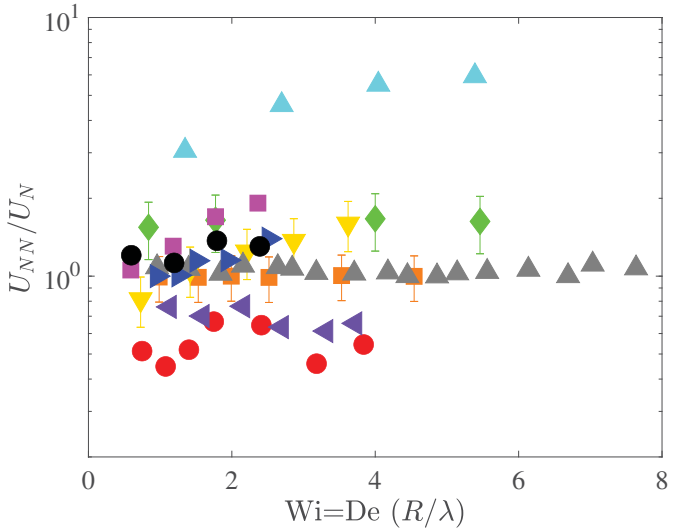

FIGURE 4.10: Ratio of viscoelastic swimming speed between viscoelastic and Newtonian fluids, U_{NN}/U_N, as a function of Weissenberg number $Wi = (R/\lambda)\,De$.

Contrasting our data with the experimental results from Liu *et al.* [53], we notice that in this work also the dependence of the swimming speeds with De number for helices with different pitch angles did not collapse into a single curve. The follow-up numerical study by Spagnolie *et al.* [48] showed also that the ratio U_{NN}/U_N was affected by both the Deborah number and the helix pitch angle. Guided by these studies, we re-plot our data in Figure 4.11 with the swimming speed increase now shown as a function of $2\pi R/\lambda = \tan\beta$, see Equation 2.12. Displayed in this manner, we see a remarkably consistent increase of swimming enhancement with R/λ (*i.e.* with the helix angle, β) regardless of the value of the Deborah number. A value of $R/\lambda \sim 0.213$, corresponding to a helix angle $\beta \sim 53.3$, appears to mark the transition from a decrease to an increase in swimming speed. We have also included the data from Liu *et al.* [53] in Figure 4.11 ($*$ and $\times$ symbols); the small number of data points in that study appear to fit within the uncertainty of our experiments. However, the increase in U_{NN}/U_N found by these authors was very modest in

comparison with the present data where we obtain increases of up to a factor of five.

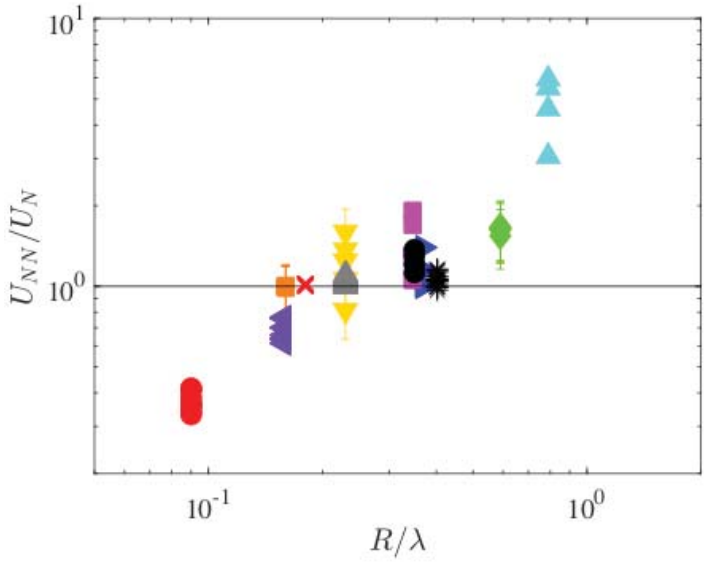

FIGURE 4.11: Ratio of viscoelastic to Newtonian swimming speed, U_{NN}/U_N, as a function of the helix aspect ratio, R/λ. The $*$ and $\times$ symbols show the data from Liu *et al.* [53].

Figure 4.11 shows that the helix-to-head size ratio, $D^* = 2R/D_H$, varies from 0.6 to 3.9. Therefore, the helix diameter can be smaller, similar or larger than the head diameter. To explore how this change in geometry affects the swimming speed, we show in Figure 4.12 the normalized swimming speed, U_{NN}/U_N, as a function of the size ratio D^*, for all the experiments conducted in this investigation. Clearly and similarly to the results in Figure 4.11, a correlation can be identified. When the head is smaller than the helix, the swimming speed in the viscoelastic fluid is larger than the Newtonian one, and when the head is larger the opposite happens.

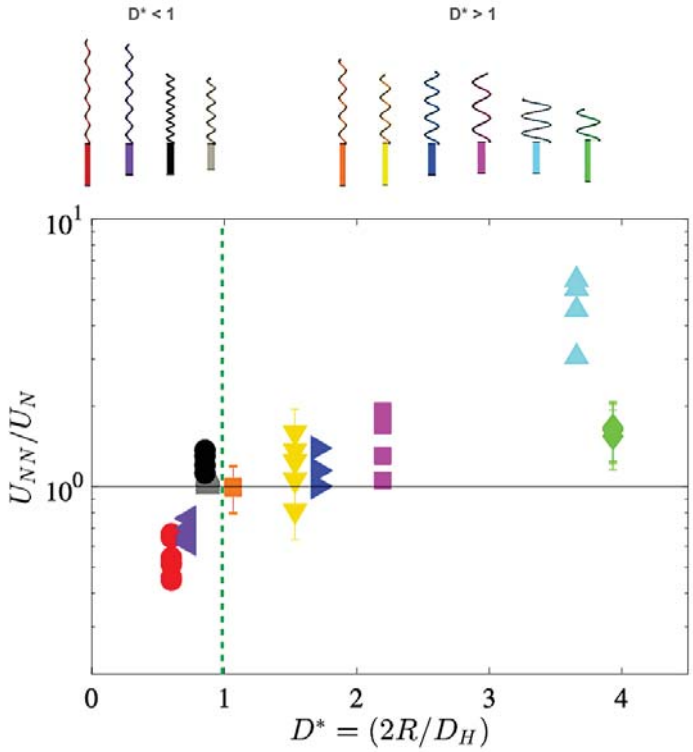

FIGURE 4.12: Ratio of viscoelastic to Newtonian swimming speed, U_{NN}/U_N, as a function of helix to head diameter ratio, $D^* = 2R/D_H$.

4.3.1. Model

We can provide a physical mechanism for the change in swimming plotted as in Figure 4.12 by turning to past work that addressed the effect of asymmetry for rotating swimmers in viscoelastic fluids. These theoretical [60] and experimental studies [61] showed that a snowman, *i.e.*, a dumbbell composed of two spheres of different diameters, could swim in a viscoelastic fluid when rotating about its symmetry axis. The physical origin of the propulsion lies in the secondary flows generated in elastic fluids by the normal-stress difference that, for a rotating sphere, leads to fluid flows directed away from the sphere along its rotation axis. A dumbbell made of two spheres of different sizes experiences therefore an imbalance of drag due to these two elastic flows, resulting in swimming. This viscoelastic propulsion force is directed in the direction from the largest to the smallest sphere [60, 61].

Our data in Figure 4.12 clearly indicate that the front-back asymmetry of the helical swimmers does control the normalized swimming speed. We

propose therefore that it is the size asymmetry between the head and the tail that leads to an additional snowman-like viscoelastic force affecting the swimming speed. If this mechanism is correct, and for locomotion that takes place head-first (the case in our experiments), a swimmer with a head smaller than the helix should swim faster due to this viscoelastic snowman effect. Conversely, if the head is larger than the tail the swimming speed should decrease. This is indeed what we see in our experiments.

To be more quantitative, we consider the theoretical expression derived in Equation 4.2. For the force balance and estimate the additional viscoelastic force resulting from the difference in size between the head and helix. Assuming as a first approximation that the additional viscoelastic force is generated regardless of the detailed shape of the head or helix, and identifying the diameters of the spheres in Ref. [60] to the diameters of the head and helix in our experiment, we can propose the snowman propulsive force as

$$F_{snow} = D_H K_s De \frac{D^{*3}(1-D^*)}{(1+D^*)^5}\omega R \tag{4.3}$$

Where K_s is viscous drag coefficient, $D^* = 2R/D_H$ is the rise ratio, and $De = \omega\tau$ is the Deborah number.

In this case, we assume an additional force due to viscoelastic force resulting from the difference in size between the head and helix that we called F_{snow}. Then the total balance forces of Equation 2.7 becomes in

$$F_{thrust} + F_{snow} = D_{helix} + D_{head} \tag{4.4}$$

For simplicity, we assume the propulsion and drag forces on the helix are not far from those given by the Newtonian resistive-force theory from Equation 2.28. In this sense, the steady force balance on the swimmer in a viscoelastic fluid is become in

$$\begin{aligned} L\sin\beta(K_\parallel - K_\perp)\omega R + D_H K_s De \frac{D^{*3}(1-D^*)}{(1+D^*)^5}\omega R = \\ L\left(K_\parallel \cos\beta + K_\perp \frac{\sin^2\beta}{\cos\beta}\right)V + K_\parallel L_H V \end{aligned} \tag{4.5}$$

Solving for the velocity V and renaming as V_{NN}, we obtain

$$V_{NN} = \omega R \frac{(\varsigma - 1)\tan\beta + \dfrac{D_H^* K_s^*}{\cos\beta} De \dfrac{D^{*3}(1-D^*)}{(1+D^*)^5}}{1 + \varsigma \tan^2\beta + \varsigma_0 L^* \sec\beta}., \tag{4.6}$$

where $\varsigma = K_\perp / K_\parallel$, $L^* = L_H / L$, $K_s^* = Ks / K_\parallel$, $D_H^* = D_H / L$ and $\varsigma_0 = D / K_\parallel$. Note that this equation is similar to the velocity for the Newtonian fluid, see Equation 2.32, but with an extra term due to the viscoelasticity. In fact, we can rewrite Equation 4.6 as the sum of Newtonian and viscoelastic contributions, as:

$$V_{NN} = \omega R \frac{(\varsigma - 1)\tan\beta}{1 + \varsigma \tan^2\beta + \varsigma_0 L^* \sec\beta} + \omega R \frac{\dfrac{D_H^* K_s^*}{\cos\beta} De \dfrac{D^{*3}(1-D^*)}{(1+D^*)^5}}{1 + \varsigma \tan^2\beta + \varsigma_0 L^* \sec\beta}. \tag{4.7}$$

We can define the viscoelastic contribution as

$$V_{elas} = \omega R \frac{\dfrac{D_H^* K_s^*}{\cos\beta} De \dfrac{D^{*3}(1-D^*)}{(1+D^*)^5}}{1 + \varsigma \tan^2\beta + \varsigma_0 L^* \sec\beta}. \tag{4.8}$$

Then taking in account the equations for the Newtonian velocity V_N, Equation 2.32, and the viscoelastic velocity V_{elas}, Equation 4.8, we can write the Equation 4.7 equivalently as

$$V_{NN} = V_N + V_{elas}. \tag{4.9}$$

Normalizing by the Newtonian velocity, the additional viscoelastic thrust resulting from the front-back asymmetry leads to the normalized swimming speed written as a sum

$$\frac{V_{NN}}{V_N} = 1 + \frac{V_{elas}}{V_N}. \tag{4.10}$$

Where

$$\frac{V_{elas}}{V_N} = D_H^* K_s^* \frac{De}{\sin\beta(\varsigma - 1)} \frac{D^{*3}(1-D^*)}{(1+D^*)^5} \tag{4.11}$$

This last expression indicates that the viscoelastic contribution due to the asymmetry of the swimmer depends on many factors, including the Deborah number and the size ratio of the head and the helix, D^*. Importantly, the ratio U_{elas}/U_N can be positive or negative depending on the value of D^* relative to one. Swimmers with $D^* > 1$ will swim faster than in the Newtonian fluid while those with $D^* < 1$ will slow down.

To show that this snowman model can reproduce the experimental trend, we use Equation 4.11 to define first a modified value of U_{elas}/U_N, termed U_S^*, as

$$U_S^* = \frac{U_{elas}}{U_N}\frac{\sin\beta}{D_H^*} = K_s^*\frac{De}{\varsigma - 1}\frac{D^{*3}(1-D^*)}{(1+D^*)^5} \tag{4.12}$$

where $\sin\beta$ and D_H^* are known quantities in the experiments.The value of U_s^* can be plotted as a function of D^* for given values of De and K_s. So, from Figure 4.9 we extract data for $De \approx 6.8$.

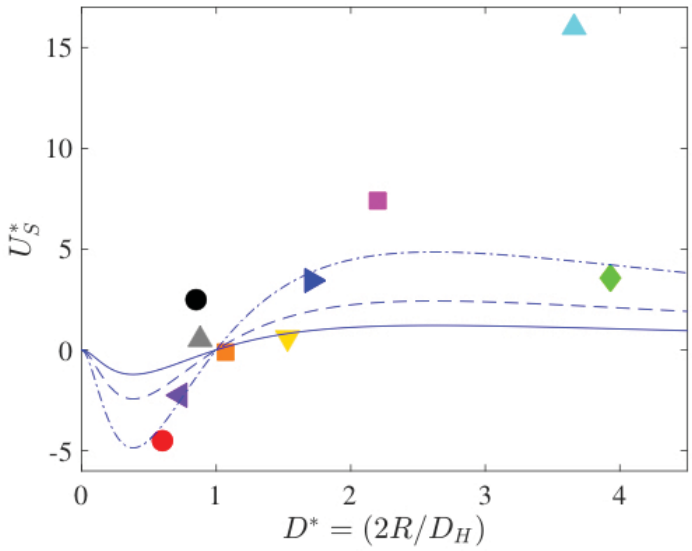

FIGURE 4.13: Modified extra swimming speed, U_S^* (defined in Equation 4.12), as a function of helix to head diameter ratio $D^* \equiv 2R/D_H$, for ≈ 6.8. The symbols are the experimental values while the lines show the theoretical predictions of the model in Equation 4.12 with values $\xi_s = 20$ (solid line), 40 (dashed line) and 80 (dash-dotted line)

We show in Figure 4.13 the comparison between the model, Equation 4.12, and the experimental values using three dimensionless values for K_s^*. The model can reproduce the experimental trend and shows a clear transition for U_{NN}/U_N from negative to positive values, thus explaining the transition from slower to faster than Newtonian when the helix to tail size ratio goes from smaller to larger than unity.

4.4. Summary and Conclusions

In this chapter, we have carried out experiments on the locomotion of free-swimming magnetically-driven rigid helices in Newtonian and

viscoelastic (Boger) fluids. We varied the sizes of the swimmer's body and its helical tail and showed that the viscoelasticity impact depends critically on the swimmer geometry: it can lead to a large increase of the swimming speed, a decrease, or can have approximately no impact. We proposed that the influence of viscoelasticity on helical propulsion is controlled by a snowman-like viscoelastic effect, previously reported for dumbbell swimmers, wherein the front-back asymmetry of the swimmer generates a non-Newtonian elastic propulsion force that can either favor or hinder locomotion.

The obvious next step in this investigation would be to address a similar question for biological swimmers propelled by helical flagellar filaments. Swimming bacteria such as E. coli have a cell body whose width is approximately $D_H \approx 0.88\ \mu m$ while the diameters of the helical flagella are approximately $2R \approx 0.4\ \mu m$. The dimensionless ratio in that cases is given by $D^* = 2R/D$ therefore that bacteria self-propelling in similar fluids would have their swimming speed decreased by elastic stresses.

Chapter 5

Helix swimming in granular mater

5.1. Introduction

In nature, many animals live on the surface of the ground. Some of these animals are undulatory crawlers, such as sand lizard and snakes. Such animals may propel themselves at twice their body length per second both under and over a sandy surfaces [19]. Frictional ground reaction forces provide thrust. Despite differences in the physical mechanisms involved, solid friction is an analog to the resistive-force theory in viscous fluid. As such, this concept has been successfully applied in the context of granular media to describe the undulatory motion of sand lizards and snakes [62, 20].

Locomotion in granular matter is less well understood due to its complex rheological features [17, 18]. For this reason accurate equations comparable to the Navier-Stokes equations for fluids have not been developed. The frictional nature of the particles results in yield stress, a threshold above which the grains flow in response to external forcing [17]. The resistance experienced by a moving intruder originates from the inhomogeneous and anisotropic response of the granular force chains. These chains are local areas affected by the surrounding grains [19]. At low locomotion speed and a granular media slightly polydisperse (to avoid segregation), where the granular matter is in a quasi-static regime, the effect of inertia is negligible when compared to frictional and gravitational forces from granular media [20, 19]. This is analogous to low Reynolds-number fluid.

Maladen *et al.* [21], inspired by RFT theory for locomotion in viscous fluids, developed an empirical RTF in locomotion of sandfish which moves in the subsurface describing a sinusoidal waveform. However, it is known that drag forces can differ depending on the physics which governs the body-medium interaction. For this reason, Maladen *et al.* [21] measured in granular substrates

the forces perpendicular $F_\perp$ and parallel $F_\parallel$ to the direction of movement for a slender cylinder and fitting some parameters, in this way they obtained the analogous version of resistant coefficients for granular media. These functions were shown effective in modeling the undulatory subsurface locomotion of sandfish. Nevertheless, the influence of geometry in the self-propulsion in granular media is an interesting topic that has not been investigated, in particular with a helical swimmer. Since then, recent studies demonstrated that helical motion is employed by *Erodium and Pelargonium* seeds to penetrate loose soils [22].

5.1.1. RTF for granular matter

In this section, we discuss under what assumptions the RTF theory can be applied to a granular medium. Also, we will discuss about the resistance coefficients for this case developed by Maladen et al. [21].

We only consider for undulatory locomotion in granular media the slow-motion regime where grain-grain and grain-swimmer frictional forces dominate material inertial forces [21, 63]. Also, we assume the swimmer motion near the surface in a horizontal plane, so the change of resistance due to depth is irrelevant. In this regime, the granular particles behave like a dense frictional fluid where the material is constantly stirred by the movement of the swimmer [63, 17]. The resistance coefficients in the Newtonian case, expressed in Equation 2.8, can be considered constant. The analogy for granular media was developed experimentally by Maladen *et al.* [21], these coefficients are in function of fitting parameters C_S and C_F, and the orientation ψ of the element to motion direction as shown in Figure 5.1,

$$F_\perp(\psi) = 2r_0(C_S \sin\beta_0 + C_F \sin\psi), \quad F_\parallel = 2r_0 C_F \cos\psi. \tag{5.1}$$

Where r_0 is the radius of the segment, $\tan\beta_0 = \cot\gamma_0 \sin\psi$, γ_0 is a constant related to the internal slip angle of the granular media [21], and ψ is the angle between the velocity vector V and tangential vector $\hat{\boldsymbol{t}}$, see Figure 5.1.

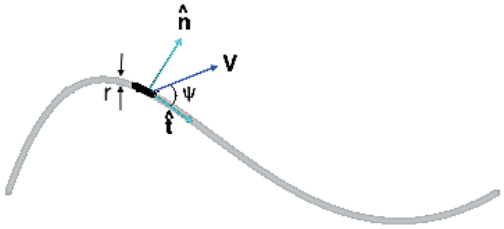

FIGURE 5.1: Sketch of the velocity V, normal $\hat{n}$, and tangential $\hat{t}$ vectors. And the angle between the velocity and tangential vectors ψ.

A key parameter in granular media is the volume fraction ϕ defined as the ratio of material volume to total occupied volume. The response of granular media to intrusion depend on ϕ, in this way C_S and C_F depends on ϕ [21]. In other words, C_S and C_F capture the contribution of the kind of granular media characterized by the volume fraction, ϕ, and the internal slip angle, γ_0. In fact, C_S and C_F have units of Kg/s^2, which in analogy with the theory of the fluids correspond to μV, where V is velocity and μ is viscosity. In this way, for each granular media we have different coefficients C_S and C_F as well as for each fluid we have different viscosities.

5.2. Experimental setup

To study the swimming dynamics in the sand, we considered the self-propulsion of a magnetic robot. The experimental design is similar to that previously used in Section 3.2.3. The swimmer consists of a magnetic head and a helical tail, it was placed in the middle of a pool filled with rigid particles. Resulting from the interaction of the rotating helix with the granular media, the robot propelled itself without being attached to a shaft or any other external structure. For more details see reference [64].

5.3. Results and discussion

In this section we present the estimation for the velocity of a helicoidal swimmer in a granular media. We link the resistance coefficients developed by Maladen *et al.* [21] in a granular media and the RTF for a helix from the Section 2.2. We estimate two cases: with and without head.

5.3.1. Speed estimation

To do a speed estimation, we should rewrite Equation 5.1. For our purposes it is necessary to remember that ψ is the angle between the velocity vector $\boldsymbol{V}$ and tangential vector $\hat{\boldsymbol{t}}$. It follows that

$$\sin\psi = \frac{\boldsymbol{V}}{\|V\|}\cdot\hat{\boldsymbol{n}} = \frac{V_\perp}{\|V\|} \quad \text{and} \quad \cos\psi = \frac{\boldsymbol{V}}{\|V\|}\cdot\hat{\boldsymbol{t}} = \frac{V_\parallel}{\|V\|}. \tag{5.2}$$

In this way we can rewrite Equation 5.1 in terms of $\sin\psi$ and $\cos\psi$, with the identity $\cos\beta_0 = (\tan^2\beta_0 + 1)^{-1/2}$ it is easy to see

$$\begin{aligned} F_\perp &= 2r_0\left(C_S\frac{\sin\beta_0}{\cos\beta_0}\frac{\cos\beta_0}{\sin\psi} + C_F\right)\sin\psi \\ &= 2r_0\left(\frac{C_S}{\sqrt{\sin^2\psi + \tan^2\gamma_0}} + C_F\right)\sin\psi \\ &= \frac{2r_0}{\|V\|}\left(\frac{C_S}{\sqrt{\sin^2\psi + \tan^2\gamma_0}} + C_F\right)V_\perp, \end{aligned} \tag{5.3}$$

$$F_\parallel = \frac{2r_0C_F}{\|V\|}V_\parallel$$

In analogy with viscous flow theory Equation 2.8 we can redefine

$$\begin{aligned} F_\perp &= K_\perp(\psi)\,V_\perp \quad \text{with} \quad K_\perp(\psi) = \frac{2r}{\|V\|}\left(\frac{C_S}{\sqrt{\sin^2\psi + \tan^2\gamma_0}} + C_F\right), \\ F_\parallel &= K_\parallel\,V_\parallel \text{with} \quad K_\parallel = \frac{2r_0C_F}{\|V\|}. \end{aligned} \tag{5.4}$$

Note that $K_\parallel$ is constant because the drag is independent of ψ, and $K_\perp$ depends on the orientation ψ of the element to motion direction. Additionally, $K_\perp$ and $K_\parallel$ have units off kg/s that in analogy with fluids theory correspond to $\mu\,d$, where μ is viscosity and d is any distance. So, we recover the meaning of $K_\perp$ and $K_\parallel$ as resistant coefficients because those are the resistance to movement by a unit of length.

From Equation 5.4, we can apply the RTF theory described in Section 2.2 for any slender body in granular media when the inertial forces are negligible. This theory was applied for sinusoidal swimmer, 2D, on the media surface by

Maladen *et al.* [21].

5.3.2. Speed without head

The force balance from Equation 2.27 considering a headless helical flagellum, we obtain

$$(K_{\parallel} - K_{\perp}) \tan\beta \, V_{\theta} + (K_{\parallel} + K_{\perp} \tan^2\beta) V_x = 0, \tag{5.5}$$

or in an equivalent way considering Equation 2.12

$$\left(1 - \frac{K_{\perp}}{K_{\parallel}}\right) R^2 k\omega + \left(1 + \frac{K_{\perp}}{K_{\parallel}} R^2 k^2\right) V_x = 0 \tag{5.6}$$

Now we need to consider the resistance coefficients for granular media from Equation 5.4 and Equation 5.5. For this, it is necessary to change ψ in these resistance coefficients in terms of the geometric parameters of the helix. Considering the equation Equation 2.10, we can find the velocity vector

$$\hat{\boldsymbol{V}} = \frac{1}{\sqrt{V_x^2 + R^2\omega^2}} \left[V_x \hat{\boldsymbol{e}}_{\boldsymbol{x}}, -\omega R \hat{\boldsymbol{e}}_{\boldsymbol{\theta}}\right]. \tag{5.7}$$

With the Equation 5.7 and Equation 2.11 we can re-express $\sin\psi$ and $\cos\psi$ from Equation 5.2

$$\cos^2\psi = \frac{(V_x - \omega R^2 k)^2}{(V_x^2 + \omega^2 R^2)(1 + R^2 k^2)}, \quad \sin^2\psi = \frac{(V_x R k + R\omega)^2}{(V_x^2 + R^2\omega^2)(1 + R^2 k^2)}. \tag{5.8}$$

Now, we can substitute $\sin\psi$ from Equation 5.8 in the expression for $K_{\perp}$ from Equation 5.4

$$K_{\perp} = 2r_0 \left(\frac{Cs \sqrt{1 + R^2 k^2}}{\sqrt{(V_x R k + R\omega)^2 + \tan^2\gamma_0 (V_x^2 + R^2\omega^2)(1 + R^2 k^2)}} + \frac{C_F}{\sqrt{V_x^2 + R^2\omega^2}} \right) \tag{5.9}$$

while for $K_{\parallel}$ only we need to consider the Equation 5.7

$$K_{\parallel} = \frac{2r_0 \, C_F}{\sqrt{V_x^2 + R^2\omega^2}}. \tag{5.10}$$

Considering the ratio between $K_\perp$ and $K_\parallel$ we obtain

$$\frac{K_\perp}{K_\parallel} = \frac{C_S}{C_F} \frac{\sqrt{1+R^2k^2}\sqrt{V_x^2+R^2\omega^2}}{\sqrt{(V_xRk+R\omega)^2+\tan^2\gamma_0(V_x^2+R^2\omega^2)(1+R^2k^2)}} + 1. \tag{5.11}$$

It is important to note that $K_\perp/K_\parallel > 1$ for all helixes in the granular media. Therefore, $K_\perp > K_\parallel$ as in theory for Newtonian fluids, Section 2.2. In other words, there is thrust because the resistance coefficients are different.

Equation 5.11 can be substituted in Equation 5.6 and we obtain a non-explicit equation for the velocity V_x. Nevertheless, we obtain an expression in powers of velocity

$$\begin{aligned}
&V_x^4\left[\frac{C_S^2}{C_F^2}R^4k^4 - R^2k^2(1+R^2k^2) - (1+R^2k^2)^2\tan^2\gamma_0\right] \\
&-2V_x^3\left[\frac{C_S^2}{C_F^2}R^4k^3\omega + R^2k\omega(1+R^2k^2)\right] \\
&+V_x^2\left[\frac{C_S^2}{C_F^2}R^4k^2\omega^2 + \frac{C_S^2}{C_F^2}R^6k^4\omega^2 - R^2\omega^2(1+R^2k^2) - \tan^2\gamma_0(1+R^2k^2)^2R^2\omega^2\right] \\
&-2V_x\left[\frac{C_S^2}{C_F^2}R^6k^3w^3\right] + \frac{C_S^2}{C_F^2}R^6k^2\omega^4 = 0.
\end{aligned} \tag{5.12}$$

An equivalent equation is obtained if we consider the helix angle β in terms of the geometrical parameters of the helix via Equation 2.12 where it is followed that $\tan\beta = Rk$,

$$\begin{aligned}
&V_x^4\left[\frac{C_S^2}{C_F^2}\tan^4\beta - \tan^2\beta(1+\tan^2\beta) - (1+\tan^2\beta)^2\tan^2\gamma_0\right] \\
&-2R\omega V_x^3\left[\frac{C_S^2}{C_F^2}\tan^3\beta + \tan\beta(1+\tan^2\beta)\right] \\
&+R^2\omega^2V_x^2\left[\frac{C_S^2}{C_F^2}\tan^2\beta + \frac{C_S^2}{C_F^2}\tan^4\beta - (1+\tan^2\beta) - \tan^2\gamma_0(1+\tan^2\beta)^2\right] \\
&-2R^3\omega^3V_x\left[\frac{C_S^2}{C_F^2}\tan^3\beta\right] + \frac{C_S^2}{C_F^2}R^4\omega^4\tan^2\beta = 0.
\end{aligned} \tag{5.13}$$

We solve for the roots of this polynomial function using Mathematica and found two real velocities, but one of these is larger than we expected. So, we selected the velocity that fit experimental data. Figure 5.2 shows the speed V_x

as a function of the angle of the helix, β, for six rotation rates. The solution from Equation 5.13 is shown in dotted lines and the points are the experimental data. For all rotation rates, the swimmer speed progressively increases with the angle of the helix, β, or analogous with the wavelength, λ, until reaches a maximum and then it decreases. In other words, there is an optimal shape of the helix for which the velocity has a maximum.

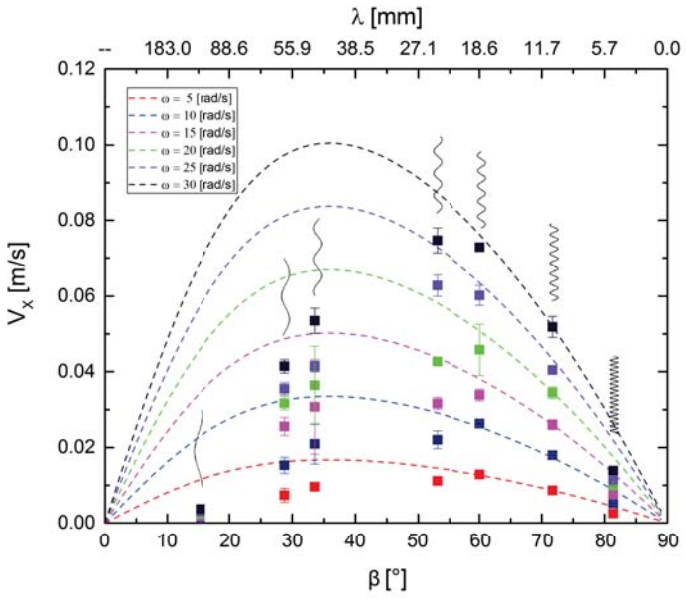

FIGURE 5.2: Swimming speed in granular medium V_x as a function of angle of the helix β and the wavelength $\lambda = 2\pi/k$ for six frequencies, ω. Dotted lines are the theoretical prediction form Equation 5.13 and points are the experimental data. Taken from R. Vazquez, 2017

For all frequencies the theory predicts the global behavior of the velocity and it fits well with the experimental points for helix angles $\beta > 60^o$. However, for small helix angles the difference between the theoretical prediction and the experimental measures for the lowest frequency, $\omega = 5\,rad/s$, is approximately 33% while for the biggest frequency, $\omega = 30\,rad/s$, is approximately 95%. Additionally, all theoretical lines start at $V_x = R^2\omega^2(1 - \tan^2\gamma_0)/\tan^2\gamma_0$ that is nearly zero. However the experimental points start near 15^o which corresponds to the internal slip angle of the granular media.

We are currently working on finding C_S^2/C_F^2 that fits the experimental data obtained in our group. In the graph of Figure 5.2 we used an approximate

value of $C_S^2/C_F^2 \approx 1.7$ reported by Madelen [21]. Also, we are developing an expression that incorporates the effect of the swimmer's head.

5.3.3. Speed with head

For the second case, we considered the head effect in the force balance Equation 2.7. Considering a cylindrical head with length L_H and the movement only in the x axis. In general, the force due to the head is

$$D_{head} = \int_0^{L_H} (F_\perp \sin\beta - F_\parallel \cos\beta)\, dx \tag{5.14}$$

Nevertheless, we will only consider the first term where the head position is normal to the movement of the swimmer. That is why we only consider the term which contains the normal force $F_\perp$, so $D_{head} = F_\perp L_H$, where $F_N = K_\perp V_x$ and K_N was define in Equation 5.9. Therefore

$$\begin{aligned} D_{head} = 2r_h L_H \Bigg(& \frac{Cs\ \sqrt{1+R^2k^2}}{\sqrt{(V_x Rk + R\omega)^2 + \tan^2\gamma_0 (V_x^2 + R^2\omega^2)(1+R^2k^2)}} \\ & + \frac{C_F}{\sqrt{V_x^2 + R^2\omega^2}} \Bigg) V_x, \end{aligned} \tag{5.15}$$

where $r_h = D_H/2$ is the radio of the head and D_H is the diameter.
On the other hand, the general balance force (see Equation 2.7) considering the head in the moving direction is the force due to the body (Equation 2.26) plus the head force (Equation 5.15)

$$F_{x_T} = \int_0^{L_T} [\sin\beta(K_\parallel - K_\perp)V_\theta + (K_\parallel \cos^2\beta + K_\perp \sin^2\beta)\frac{V_x}{\cos\beta}]\, dx + D_{head}. \tag{5.16}$$

Considering Equation 2.12, it is easy to see that

$$F_{x_T} = \frac{K_\perp}{K_\parallel} R^2 k(kV_x - \omega) + (V_x + R^2 k\omega) + D_{head}\frac{\sqrt{1+R^2k^2}}{LK_\parallel} = 0 \tag{5.17}$$

Taking in to account the expressions corresponding to $K_\perp$ and $K_\parallel$ in Equation 5.9, Equation 5.10 and Equation 5.11. After some algebra, we can obtain an expression in powers of velocity

$$
\begin{aligned}
&V_x^4\left\{\frac{C_S^2}{C_F^2}\tan^4\beta-\tan^2\beta\sec^2\beta-\sec^4\beta\tan^2\gamma_0\right.\\
&+2\frac{L_H}{L_T}\frac{D_H}{2a}\sec\beta\left[\tan^2\beta+\sec^2\beta\tan^2\gamma_0-\frac{C_S^2}{C_F^2}\tan^2\beta\right]\\
&\left.+\frac{L_H^2}{L_T^2}\frac{D_H^2}{4a^2}\left[\frac{C_S^2}{C_T^2}\sec^2\beta-\tan^2\beta-\tan^2\gamma_0\sec^2\beta\right]\right\}\\
&+2R\omega V_x^3\tan\beta\left\{-\left[\frac{C_S^2}{C_F^2}\tan^2\beta+\sec^2\beta\right]+\frac{L_H}{L_T}\frac{D_H}{2a}\sec\beta\left[2-\frac{C_S^2}{C_F^2}\right]-\frac{L_H^2}{L_T^2}\frac{D_H^2}{4a^2}\right\}\\
&+R^2\omega^2V_x^2\left\{\sec^2\beta\left(\frac{C_S^2}{C_F^2}\tan^2\beta-1-\tan^2\gamma_0\sec^2\beta\right)\right.\\
&-2\frac{L_H}{L_T}\frac{D_H}{2a}\sec\beta\left[\frac{C_S^2}{C_F^2}\tan^2\beta+1+\tan^2\gamma_0\sec^2\beta\right]\\
&\left.+\frac{L_H^2}{L_T^2}\frac{D_H}{2a}\left[\frac{C_S^2}{C_F^2}\sec^2\beta-\tan^2\gamma_0\sec^2\beta-1\right]\right\}\\
&-2R^3\omega^3V_x\left[\frac{C_S^2}{C_F^2}\tan^3\beta+\frac{L_H}{L_T}\frac{D_H}{2a}\frac{C_S^2}{C_F^2}\tan\beta\sec\beta\right]+\frac{C_S^2}{C_F^2}R^4\omega^4\tan^2\beta=0.
\end{aligned}
\tag{5.18}
$$

Observe that Equation 5.18 recovers the headless case when the length of the head L_H tends to zero, see Equation 5.13.

We used Mathematica to obtain the graphic solution to Equation 5.18. For the range of parameters corresponding to our study, two real and two complex roots are found. The smaller real root is used, since it is closer to experimental results. As seen in Figure 5.3, the experimental measurements and the predictions (lines) agree very well qualitatively and quantitatively. It shows that the swimming speed has a maximum. The prediction underestimates the experimental results, for about 30% for large helix angles, β. Also, the angle at which the swimming speed is maximum is around 55^o while the model predicts 30^o.

Finally, for small angles of the helix the swimmer rotates around its axis in all experiments but does not move forward. However, this threshold angle is not reproduced by the model because it is an extension of the RTF in which there are no minimum conditions for swimming such as a yield stress. In other words, such a critical angle is intrinsic of the granular media.

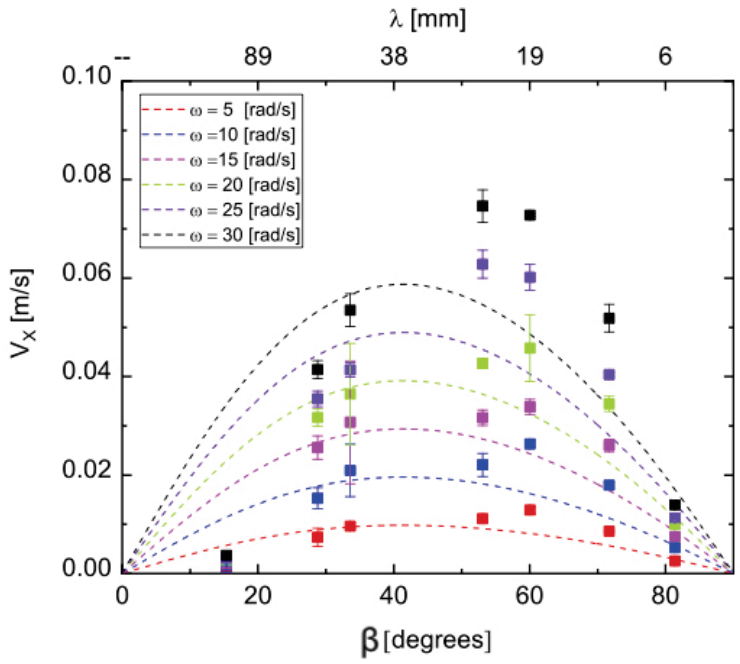

FIGURE 5.3: Swimming speed in granular medium V_x as a function of angle of the helix β and the wavelength $\lambda = 2\pi/k$ for six frequencies ω. Dotted lines are the theoretical prediction form Equation 5.18 and points are the experimental data. Taken from R. Vazquez, 2017

We should mention that the theoretical lines depend on the coefficients C_s, C_f which were taken from Madelen's article [21]. The granular medium used for the experiments is similar to that used by Madelen. However, it is not exactly the same, so newly calculated coefficients may improve the curve fit.

5.4. Summary and conclusions

The motility of free helical swimmers in granular media is studied experimentally. The geometrical characteristics of the swimmer robots, which represent an advantage in swimming ability, were obtained. The extension of the granular RFT theory to consider the rigid helical tail produced a model for which predictions showed a good agreement with our experimental data. The model also captured the order of magnitud of several other features of the experiments in magnitude order. But two important aspects were not captured: the first aspect involves the minimum conditions for motion and the angle at which the velocity is a maximum. We found that, for small angles of the helix, the swimmer rotates around its axis, but does not move forward. It appears that an angle threshold should exist. Second, the experiments showed that a

helix angle of approximately 55^o results in a maximum normalized speed; in contrast, the granular RFT predicts a smaller angle for the fastest swimming (about 30^o). The present experimental campaign contributes to the current discussion on locomotion in granular media and further validates the granular RFT modeling.

Chapter 6

Conclusions

In this thesis, I presented an investigation about swimming in complex fluids such as Boger fluids and granular mater. This topic has both a practical and a scientific relevance. It has many applications in human health, ecological systems, animal locomotion, etc. This thesis makes a contribution to understand swimming in Boger fluids and granular matter, and the effect of boundaries in swimming speed for a helical swimmer. As we discussed before there are some questions about how organism exploit the fluid internal structure or the boundaries for propulsion.

This thesis shows experimentally that the swimming speed increases with confinement for all frequencies in both fluids: Newtonian and viscoelastic. In other words, the walls (confinement) help to increase the swimming velocity. Additionally, we find that fluid elasticity increases the propulsion of the helical swimmer. So, we derived analytically that there is an additional force in viscoelastic media that increases the speed. This is an important achievement since only result of numerical simulations were reported on the subject.

In this sense, we studied the swimming speed only in a Boger fluid varying the sizes of the swimmer body and its helical tail and showed for first time that the impact of viscoelasticity depends critically on the geometry of the swimmer: it can lead to a large increase of the swimming speed, a decrease or it may have approximately no impact. We proposed that the additional force of viscoelasticity on helical propulsion is controlled by a snowman-like viscoelastic effect, previously reported for dumbbell swimmers, wherein the front-back asymmetry of the swimmer generates a non-Newtonian elastic propulsion force that can either favor or hinder locomotion.

Finally, for the firs time we applied the RFT on the motility of free helical swimmers in granular media. The extension of the granular RFT theory shows

that it is necessary to take in account the head in the model of a rigid helical tail. Model predictions showed a good agreement with experimental data. Meaning that it captured the order of magnitud of several features of the experiments, but two important aspects were not captured. The first aspect involves the minimum conditions for motion and the angle at which the velocity is a maximum. We found that, for small angles of the helix, the swimmer rotates around its axis, but does not move forward. It appears that an angle threshold should exist. Second, the experiments showed that a helix angle of approximately 55^o results in a maximum normalized speed; in contrast, the granular RFT predicts a smaller angle for the fastest swimming (about 30^o). The present experimental campaign contributes to the current discussion on locomotion in granular media and further validates the granular RFT modeling.

Bibliography

[1] R. Dreyfus et al. “Microscopic artificial swimmers”. In: *Nature* 437.7060 (2005), pp. 862–865.

[2] L. Zhang et al. “Artificial bacterial flagella: Fabrication and magnetic control”. In: *Appl Phys Lett* 94.6 (2009), p. 064107.

[3] S. J. Ebbens and J. R. Howse. “Direct observation of the direction of motion for spherical catalytic swimmers”. In: *Langmuir* 27.20 (2011), pp. 12293–12296.

[4] C. D. Harvell et al. “Emerging marine diseases–climate links and anthropogenic factors”. In: *Science* 285.5433 (1999), pp. 1505–1510.

[5] J. W. Costerton, P. S. Stewart, and E. P. Greenberg. “Bacterial biofilms: a common cause of persistent infections”. In: *Science* 284.5418 (1999), pp. 1318–1322.

[6] G. Taylor. “Analysis of the swimming of microscopic organisms”. In: vol. 209. 1099. The Royal Society. 1951, pp. 447–461.

[7] J. J. Gray and G. J. Hancock. “The propulsion of sea-urchin spermatozoa”. In: *J. Exp. Biol.* 32.4 (1955), pp. 802–814.

[8] R. E. Johnson and C. J. Brokaw. “Flagellar hydrodynamics. A comparison between resistive-force theory and slender-body theory”. In: *Biophys. J* 25.1 (1979), pp. 113–127.

[9] D. B. Seo et al. “Development of sorting, aligning, and orienting motile sperm using microfluidic device operated by hydrostatic pressure”. In: *Microfluidics Nanofluidics* 3.5 (2007), pp. 561–570.

[10] M. A. Sleigh, J. R. Blake, and N. Llron. “State of Art”. In: *Am Rev Respir Dis* 137 (1988), pp. 726–741.

[11] G. J. Elfring and E. Lauga. “Theory of locomotion through complex fluids”. In: *Complex fluids in biological systems*. Springer, 2015, pp. 283–317.

[12] JM Dealy. “Weissenberg and Deborah numbers—their definition and use”. In: *Rheol. Bull* 79.2 (2010), pp. 14–18.

[13] G. R. Fulford, D. F. Katz, and R. L. Powell. “Swimming of spermatozoa in a linear viscoelastic fluid”. In: *Biorheology* 35.4-5 (1998), pp. 295–309.

[14] E. Lauga. “Propulsion in a viscoelastic fluid”. In: *Phys. Fluids* 19.8 (2007), p. 083104.

[15] J. Teran, L. Fauci, and M. Shelley. “Viscoelastic fluid response can increase the speed and efficiency of a free swimmer”. In: *Phys. Rev. Lett.* 104.3 (2010), p. 038101.

[16] L. Li and S. E. Spagnolie. “Swimming and pumping by helical waves in viscous and viscoelastic fluids”. In: *Phys. Fluids* 27.2 (2015), p. 021902.

[17] D. I. Goldman. “Colloquium: Biophysical principles of undulatory self-propulsion in granular media”. In: *Rev. Mod. Phys* 86.3 (2014), p. 943.

[18] T. Zhang and D. I. Goldman. “The effectiveness of resistive force theory in granular locomotion a”. In: *Phys. Fluids* 26.10 (2014), p. 101308.

[19] B. D. Texier, A. Ibarra, and F. Melo. “Helical locomotion in granular media”. In: *arXiv preprint arXiv:1707.03305* (2017).

[20] Y. Ding et al. “Mechanics of undulatory swimming in a frictional fluid”. In: *PLoS Comput. Biol* 8.12 (2012), e1002810.

[21] R. D. Maladen et al. “Undulatory swimming in sand: subsurface locomotion of the sandfish lizard”. In: *Science* 325.5938 (2009), pp. 314–318.

[22] Wonjong Jung et al. “Reduction of granular drag inspired by self-burrowing rotary seeds”. In: *Physics of Fluids* 29.4 (2017), p. 041702.

[23] E. M. Lifshitz and L. D. Landau. *Fluid mechanics: Volume 6 (course of theoretical physics)*. 1987.

[24] S. Chattopadhyay et al. “Swimming efficiency of bacterium Escherichiacoli”. In: *Proc Natl Acad Sci* 103.37 (2006), pp. 13712–13717.

[25] G. J. Hancock. “The self-propulsion of microscopic organisms through liquids”. In: *Proc R. Soc. A*. Vol. 217. 1128. The Royal Society. 1953, pp. 96–121.

[26] R. E. Johnson. “An improved slender-body theory for Stokes flow”. In: *J. Fluid Mech* 99.2 (1980), pp. 411–431.

[27] S. E. Spagnolie. “Complex fluids in biological systems”. In: *BMP, Biomedical Engineering* (2015).

[28] S. J. Lighthill. *Mathematical biofluiddynamics*. SIAM, 1975.

[29] L Gary Leal. *Advanced transport phenomena: fluid mechanics and convective transport processes*. Vol. 7. Cambridge University Press, 2007.

[30] Christopher W Macosko. "Rheology Principles". In: *Measurements and Applications* (1994).

[31] Ronald G Larson. *The structure and rheology of complex fluids*. Vol. 150. Oxford university press New York, 1999.

[32] Raja Ramesh Huilgol and Nhan Phan-Thien. *Fluid mechanics of viscoelasticity: general principles, constitutive modelling, analytical and numerical techniques*. Elsevier, 1997.

[33] KP Jackson, K Walters, and RW Williams. "A rheometrical study of Boger fluids". In: *Journal of Non-Newtonian Fluid Mechanics* 14 (1984), pp. 173–188.

[34] M. Baumgaertel and H. H. Winter. "Determination of discrete relaxation and retardation time spectra from dynamic mechanical data". In: *Rheol. Acta* 28.6 (1989), pp. 511–519.

[35] D. F. Katz. "On the propulsion of micro-organisms near solid boundaries". In: *J. Fluid. Mech.* 64.01 (1974), pp. 33–49.

[36] L. Zhu, E. Lauga, and L. Brandt. "Low-Reynolds-number swimming in a capillary tube". In: *J. Fluid. Mech.* 726 (2013), pp. 285–311.

[37] R. Ledesma-Aguilar and J. M. Yeomans. "Enhanced motility of a microswimmer in rigid and elastic confinement". In: *Phys. Rev. Lett.* 111.13 (2013), p. 138101.

[38] B. Liu, K. S. Breuer, and T. R. Powers. "Propulsion by a helical flagellum in a capillary tube". In: *Phys. Fluids* 26.1 (2014), p. 011701.

[39] B. U. Felderhof. "Swimming at low Reynolds number of a cylindrical body in a circular tube". In: *Physics of Fluids* 22.11 (2010), p. 113604.

[40] Alperen Acemoglu and Serhat Yesilyurt. "Effects of geometric parameters on swimming of micro organisms with single helical flagellum in circular channels". In: *Biophysical journal* 106.7 (2014), pp. 1537–1547.

[41] E. Demir and S. Yesilyurt. "Low Reynolds number swimming of helical structures in circular channels". In: *J. Fluids Struct* 74 (2017), pp. 234–246.

[42] S. Jana, S. H. Um, and S. Jung. "Paramecium swimming in capillary tube". In: *Phys. Fluids* 24.4 (2012), p. 041901.

[43] H. Wu et al. "Amoeboid motion in confined geometry". In: *Phys. Rev. E* 92.5 (2015), p. 050701.

[44] F.A. Godínez, O. Chávez, and R Zenit. "Note: Design of a novel rotating magnetic field device". In: *Rev. Sci. Instrum.* 83.6 (2012), p. 066109.

[45] G. J. Li, A. Karimi, and A. M. Ardekani. "Effect of solid boundaries on swimming dynamics of microorganisms in a viscoelastic fluid". In: *Rheologica acta* 53.12 (2014), pp. 911–926.

[46] L. J. Fauci and A. McDonald. "Sperm motility in the presence of boundaries". In: *B. Math. Biol.* 57.5 (1995), pp. 679–699.

[47] F. A. Godínez et al. "Complex fluids affect low-Reynolds number locomotion in a kinematic-dependent manner". In: *Exp. Fluids* 56.5 (2015), p. 97.

[48] S. E. Spagnolie, B. Liu, and T. R. Powers. "Locomotion of helical bodies in viscoelastic fluids: enhanced swimming at large helical amplitudes". In: *Phys. Rev. Lett* 111.6 (2013), p. 068101.

[49] Eric Lauga and Thomas R Powers. "The hydrodynamics of swimming microorganisms". In: *Reports on Progress in Physics* 72.9 (2009), p. 096601.

[50] Eric Lauga. "Bacterial hydrodynamics". In: *Annual Review of Fluid Mechanics* 48 (2016), pp. 105–130.

[51] Edward M Purcell. "The efficiency of propulsion by a rotating flagellum". In: *Proceedings of the National Academy of Sciences* 94.21 (1997), pp. 11307–11311.

[52] Bruce Rodenborn, Ruy Ibanez, and Harry L Swinney. "Laboratory Observation of Stratorotational Instability with a Large Density Gradient". In: *APS Division of Fluid Dynamics Meeting Abstracts*. 2013, pp. L32–010.

[53] B. Liu, T. R. Powers, and K. S. Breuer. "Force-free swimming of a model helical flagellum in viscoelastic fluids". In: *Proc. Natl. Acad. Sci* 108.49 (2011), pp. 19516–19520.

[54] X. N. Shen and P. E. Arratia. "Undulatory swimming in viscoelastic fluids". In: *Phys. Rev. Lett* 106.20 (2011), p. 208101.

[55] DA Gagnon, XN Shen, and PE Arratia. "Undulatory swimming in fluids with polymer networks". In: *EPL (Europhysics Letters)* 104.1 (2013), p. 14004.

[56] Julian Espinosa-Garcia, Eric Lauga, and Roberto Zenit. "Fluid elasticity increases the locomotion of flexible swimmers". In: *Physics of Fluids* 25.3 (2013), p. 031701.

[57] Moumita Dasgupta et al. “Speed of a swimming sheet in Newtonian and viscoelastic fluids”. In: *Physical Review E* 87.1 (2013), p. 013015.

[58] T. K. Chaudhury. “On swimming in a visco-elastic liquid”. In: *J. Fluid Mech* 95.1 (1979), 189–197. DOI: 10.1017/S0022112079001415.

[59] E. E. Riley and E. Lauga. “Enhanced active swimming in viscoelastic fluids”. In: *EPL* 108.3 (2014), p. 34003.

[60] On Shun Pak et al. “Micropropulsion and microrheology in complex fluids via symmetry breaking”. In: *Physics of fluids* 24.10 (2012), p. 103102.

[61] J Amadeus Puente-Velázquez et al. “Viscoelastic propulsion of a rotating dumbbell”. In: *Microfluidics and Nanofluidics* 23.9 (2019), p. 108.

[62] R. D. Maladen et al. “Mechanical models of sandfish locomotion reveal principles of high performance subsurface sand-swimming”. In: *J. Royal Soc. Interface* 8.62 (2011), pp. 1332–1345.

[63] Z. Peng, O. S. Pak, and G. J. Elfring. “Characteristics of undulatory locomotion in granular media”. In: *Phys. Fluids* 28.3 (2016), p. 031901.

[64] Rogelio Valdés et al. “Self-propulsion of a helical swimmer in granular matter”. In: *Physical Review Fluids* 4.8 (2019), p. 084302.